

The Circumnuclear Disk Revealed by ALMA. I. Dense Clouds and Tides in the Galactic Center

PEI-YING HSIEH,^{1,2,3} PATRICK M. KOCH,³ WOONG-TAE KIM,⁴ SERGIO MARTÍN,^{1,2} HSI-WEI YEN,³ JOHN CARPENTER,¹
NANASE HARADA,⁵ JEAN L. TURNER,⁶ PAUL T. P. HO,^{3,7} YA-WEN TANG,³ AND SARA C. BECK⁸

¹Joint ALMA Observatory, Alonso de Córdova, 3107, Vitacura, Santiago 763-0355, Chile

²European Southern Observatory, Alonso de Córdova, 3107, Vitacura, Santiago 763-0355, Chile

³Academia Sinica Institute of Astronomy and Astrophysics, P.O. Box 23-141, Taipei 10617, Taiwan, R.O.C.

⁴Department of Physics & Astronomy, Seoul National University, 1 Gwanak-ro, Gwanak-gu, Seoul 08826, Republic of Korea

⁵National Astronomical Observatory of Japan, 2-21-1 Osawa, Mitaka, Tokyo 181-8588, Japan

⁶Department of Physics and Astronomy, UCLA, Los Angeles, CA 90095-1547

⁷East Asian Observatory, 660 N. Aohoku Place, University Park, Hilo, Hawaii 96720, U.S.A.

⁸School of Physics and Astronomy, Tel Aviv University, Ramat Aviv, Israel

(Received Feb 5, 2021; Revised March 25, 2021; Accepted April 1, 2021)

Submitted to ApJ

ABSTRACT

Utilizing the Atacama Large Millimeter/submillimeter Array (ALMA), we present CS line maps in five rotational lines ($J_u = 7, 5, 4, 3, 2$) toward the circumnuclear disk (CND) and streamers of the Galactic Center. Our primary goal is to resolve the compact structures within the CND and the streamers, in order to understand the stability conditions of molecular cores in the vicinity of the supermassive black hole (SMBH) Sgr A*. Our data provide the first homogeneous high-resolution ($1.3'' = 0.05$ pc) observations aiming at resolving density and temperature structures. The CS clouds have sizes of 0.05–0.2 pc with a broad range of velocity dispersion ($\sigma_{\text{FWHM}} = 5 - 40$ km s⁻¹). The CS clouds are a mixture of warm ($T_k \geq 50 - 500$ K, $n_{\text{H}_2} = 10^{3-5}$ cm⁻³) and cold gas ($T_k \leq 50$ K, $n_{\text{H}_2} = 10^{6-8}$ cm⁻³). A stability analysis based on the unmagnetized virial theorem including tidal force shows that 84^{+16}_{-37} % of the total gas mass is tidally stable, which accounts for the majority of gas mass. Turbulence dominates the internal energy and thereby sets the threshold densities 10–100 times higher than the tidal limit at distance ≥ 1.5 pc to Sgr A*, and therefore, inhibits the clouds from collapsing to form stars near the SMBH. However, within the central 1.5 pc, the tidal force overrides turbulence and the threshold densities for a gravitational collapse quickly grow to $\geq 10^8$ cm⁻³.

Keywords: Galaxy: center — radio lines: ISM — ISM: molecules — Galaxy: structure — techniques: image processing

1. INTRODUCTION

1.1. Molecular Inflows in the Galactic Center

The mechanisms that transport molecular inflows from kilo-pc down to a few pc are a key problem in galaxy evolution, with an ultimate goal of understanding the co-evolution of inflows, star formation, and the active cycle of a supermassive black hole (SMBH) in a galaxy (e.g. Collin & Zahn 1999; Hopkins & Quataert 2010; Kim et al. 2012). The gravitational torque ex-

erted on the gas by a stellar bar has often been invoked to drive the inflows onto a kilo-pc and hundred-pc disk or ring (e.g., Athanassoula 1992; Sakamoto et al. 1999; Hsieh et al. 2011; Lin et al. 2013; Sormani & Barnes 2019; Tress et al. 2020). Within the central few pc, previous observations show that the concentration of molecular gas is influenced by the gravitational potential of a SMBH and follows a quasi-Keplerian rotation, which is often called the circumnuclear disk/ring (CND/CNR, e.g. Martín et al. 2012; Liu et al. 2012; Mills et al. 2013; Hsieh et al. 2017; Imanishi et al. 2018; Tsuboi et al. 2018; Goicoechea et al. 2018; Izumi et al. 2018; Combes et al. 2019). The CND/CNR, being the largest and closest

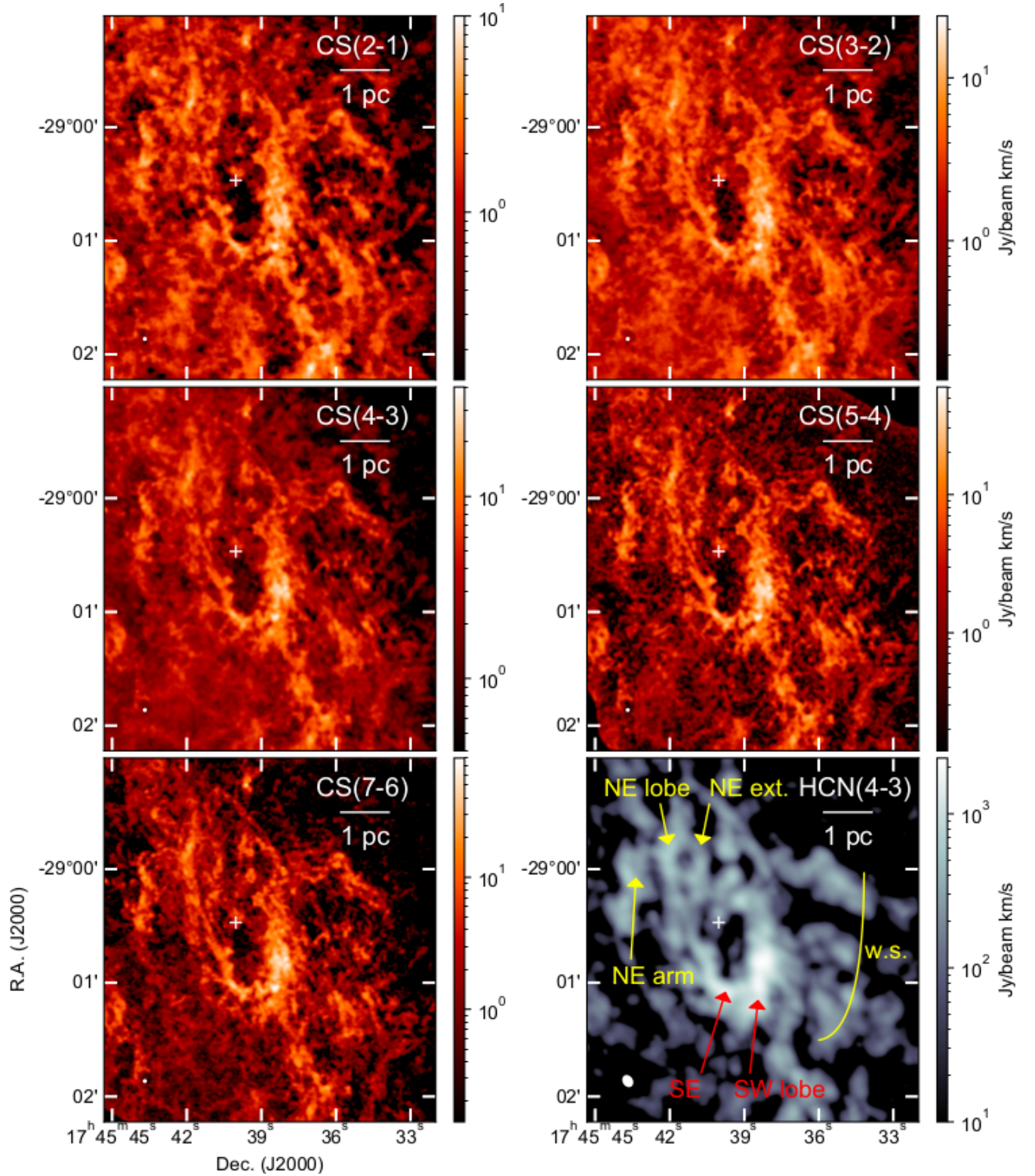


Figure 1. Upper: ALMA integrated intensity maps of CS(2-1), CS(3-2), CS(4-3), CS(5-4), and CS(7-6) tracing the CND and the streamers. Nomenclature of previously identified features in [Christopher et al. \(2005\)](#); [Montero-Castaño et al. \(2009\)](#); [Martín et al. \(2012\)](#) are labeled on the SMA HCN(4-3) map ([Liu et al. 2012](#)). The location of Sgr A* is labeled with the cross. The beam sizes are shown with the white ellipse (lower left corner), which are $1.3''$ and $5.8'' \times 4.4''$ for the ALMA and SMA maps, respectively. Scale bar of 1 pc is labeled.

molecular structure to the SMBH, is critical to under-

stand fueling of both the SMBH and the nuclear star

formation (e.g. see [Levin & Beloborodov 2003](#); [Trani et al. 2018](#), and references therein). The interplay between black hole feeding and star formation is therefore of paramount importance in the life-cycle of galaxies.

The CND of the Galactic Center (GC) is a molecular ring rotating with respect to the SMBH Sgr A*. It has an uncertain gas mass between $10^4 - 10^6 M_\odot$ ([Christopher et al. 2005](#); [Requena-Torres et al. 2012](#)) and a size of ~ 2 pc, within which are the ionized streamers called mini-spiral (or Sgr A West; [Roberts & Goss 1993](#); [Paumard et al. 2004](#); [Zhao et al. 2009](#)) and nuclear star clusters ([Figer et al. 1999](#)). Since Sgr A* is the closest SMBH, the CND in the GC therefore allows for the best spatial resolution to study the accretion processes in the local universe. The dynamical formation and destruction of the CND determines the lifetime of the cold gas accretion surrounding Sgr A*. It has been well recognized that the tidal shear from the central potential is quickly rising within the central 10 pc ([Güsten & Downes 1980](#); [Genzel et al. 1985](#); [Jackson et al. 1993](#); [Shukla et al. 2004](#); [Christopher et al. 2005](#)). The molecular clouds cannot withstand tidal disruption if their densities are lower than the tidal limit, which is 10^7 cm^{-3} at a distance of 2 pc from Sgr A*. Therefore, gas density measurements are crucial to understand whether the CND is stable and survives several orbital timescales ($\geq 10^5$ yr). The gas densities estimated by the virial equilibrium for individual clumps range from 10^6 to 10^8 cm^{-3} in earlier interferometric observations ([Shukla et al. 2004](#); [Christopher et al. 2005](#); [Montero-Castaño et al. 2009](#)). These virial densities are inconsistent with lower densities inferred from excitation analyses of spectral lines from single-dish observations (10^4 to 10^6 cm^{-3} ; [Genzel et al. 1985](#); [Marr et al. 1993](#); [Bradford et al. 2005](#); [Requena-Torres et al. 2012](#); [Mills et al. 2013](#)) and from dust observations ([White et al. 2003](#)). Lower densities and masses are also reported in a recent ALMA observation ([Tsuboi et al. 2018](#)). Hence, these inconsistencies lead to different conclusions regarding the lifetime of the CND. However, the discrepancy between the density measurements might be the result of different observed scales in this complicated region ([Requena-Torres et al. 2012](#); [Mills et al. 2013](#); [Harada et al. 2015](#)). The high resolution, sensitivity, and total power offered by ALMA allows us to revisit the measurements of physical properties of molecular clouds in the central parsecs of the GC.

The CND is not an isolated feature. The molecular gas surrounding the CND is resolved into multiple filaments with sizes $\sim 2 \text{ pc} \times 0.5 \text{ pc}$ in the HCN(4-3) map (SubMillimeter Array; SMA) ([Montero-Castaño et al. 2009](#); [Liu et al. 2012](#)). Various molecular tracers also

reveal a very clumpy distribution along the CND. The southern part of the CND is brighter than the northern part. These streamers originate from the ambient clouds 20-pc further out, and connect to the central 2 pc of the CND ([Hsieh et al. 2017](#)). The streamers are carrying gas toward the CND and end up co-rotating with the CND. This kinematic analysis suggests that these streamers show a signature of “infalling” motions with progressively higher velocities as they approach the CND. The radial inward velocity is later indirectly confirmed by the magnetic field configurations accounting for the observed dust polarization maps ([Hsieh et al. 2018](#)). These results suggest that the CND might have formed during tidal passages of nearby clouds. The broad linewidth of individual protrusions may also indicate the tidal stretching effect, i.e., the filaments are torn apart by the central gravity. This suggests that the streamers may be unstable and are dissolving at parsec-scale. These streamers contain numerous compact dense cores with sizes of 0.05 pc in the previous ALMA map ([Hsieh et al. 2019](#)). The next question is if these dense cores can survive the tidal disruption on their way of accretion onto the CND. Moreover, determining whether these compact cores are prone to star formation near Sgr A* is also important to understand both the nature of the nuclear star clusters as well as the star formation process in a highly-dynamic environment around a SMBH.

1.2. Objectives of the ALMA Observations

We have observed the CND and streamers with ALMA ([Hsieh et al. 2019](#)). Here we report a study of cloud clump properties within the inner 10 pc of the GC using millimeter and submillimeter lines of CS molecule. With these observations we can infer densities, kinetic temperatures and column densities for the clumps. With these data we can do a tidal stability analysis of the clouds to determine their likelihood of collapse. Utilizing the multiple CS transitions, we are able to measure the densities and sizes of the compact cores to derive a “surviving fraction” as a function of distance from Sgr A*. We can also probe the stability conditions of the compact cores in order to reveal the star formation conditions near a SMBH. Using the total power observation, we can determine the gas mass of the CND and streamers for the first time without previous assumptions to quantify the importance of the inflows and SMBH feeding. We have observed the CND and the streamers with the CS(7-6), (5-4), (4-3), (3-2), (2-1) lines in order to detect the dense gas accreting onto the CND. Multiple transitions with the same species are the key to determine the excitation conditions (e.g.,

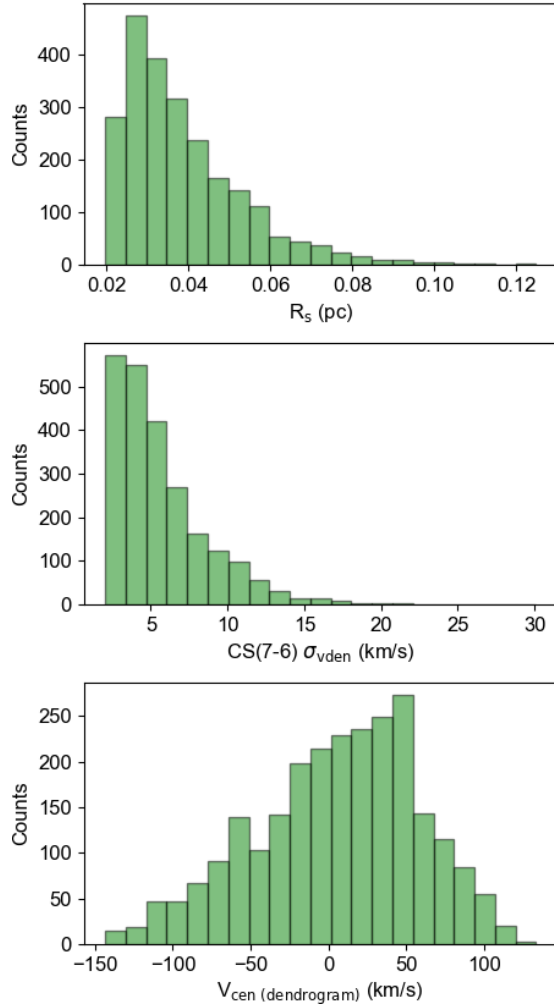


Figure 2. Histograms of the effective spherical radius R_s , rms linewidth (σ_{vden}), and velocities of clumps identified with CS(7-6) line in astrodendro. The total number of identified clumps is 2379.

Requena-Torres et al. 2012; Harada et al. 2015). The high-excitation lines minimize the self-absorption observed in lower transitions and more reliably sample the CND (Montero-Castaño et al. 2009; Tsuboi et al. 1999; Christopher et al. 2005; Wright et al. 2001). CS is an ideal tracer to achieve the above listed objectives. CO, the second most abundant molecule is affected by foreground absorption even at $J=4-3$ (Requena-Torres et al. 2012). HCN, although commonly used to trace dense gas, is easily excited by infrared radiation (Mills et al. 2013) or by electrons in some cases (Goldsmith & Kauffmann 2017). Hence, HCN is no longer a preferred density tracer. CS is abundant and a more robust dense-gas tracer ($n_{\text{H}_2} = 10^{5-7} \text{ cm}^{-3}$) than HCN and is more UV-resistant (Martín et al. 2012). We will use a radiative transfer model (RADEX) (van der Tak et al. 2007) to derive the physical parameters. A detailed comparison

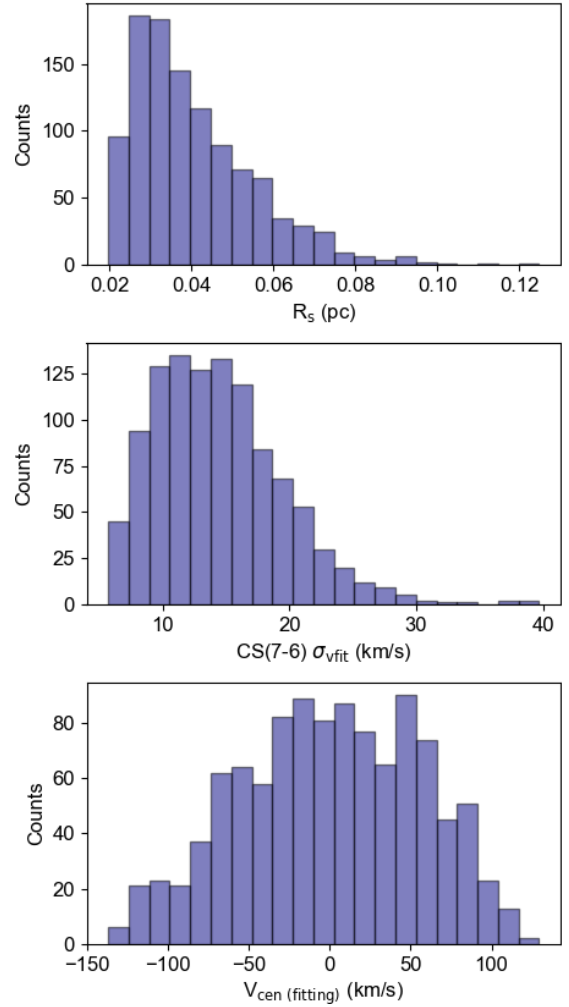


Figure 3. Histograms of the effective spherical radius R_s derived from astrodendro, rms linewidth (σ_{vfit}), and velocities of clumps identified with the CS(7-6) line with Gaussian fitting. The latter two parameters (σ_{vfit} and $V_{\text{cen (fitting)}}$) are derived from Gaussian fitting of spectra extracted at a leaf position. The selection criterion for the fitting higher than 3σ is applied. This results in 1071 clumps, which is used for radex calculation. Gaussian fit to linewidth leads to larger linewidths than the astrodendro fit, see text.

of individual structures and kinematics will be presented in forthcoming papers.

2. ALMA OBSERVATIONS AND DATA REDUCTION

ALMA observations toward the central $3'$ of the GC were carried out using the 12m array and the total-power array (project code: 2017.1.00040.S; PI: Pei-Ying Hsieh). The total on source integration times are 7, 26, 60 hours for the 12-m array, the 7-m array, and single dish observations. We have observed the CS(7-6)

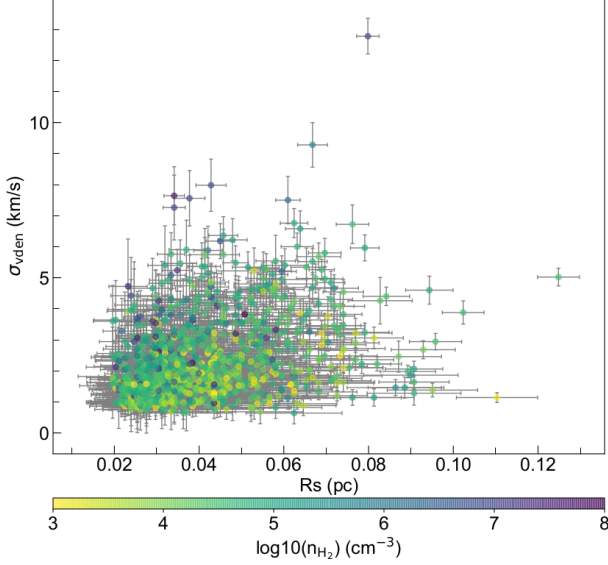


Figure 4. Size-linewidth relation of the 1071 clumps are shown. R_s and σ_{vden} are shown in the x-axis and y-axis, respectively. Colors represent n_{H_2} derived in the later section.

($f_{rest} = 342.882$ GHz), CS(5-4) ($f_{rest} = 244.935$ GHz), CS(4-3) ($f_{rest} = 195.954$ GHz), CS(3-2) ($f_{rest} = 146.969$ GHz), and CS(2-1) ($f_{rest} = 97.980$ GHz) lines (see Table 1). The default channel resolutions of the spectral windows are listed in Table 2. The observations consisted of a single field of a 68-pointing mosaic for CS(2-1) and 138 pointings CS(3-2). Two fields consisting of 251 and 300 pointings are performed to observe the CS(4-3) and CS(5-4) lines, respectively. Four fields consisting of CS(7-6) (600 pointing in total) are observed to cover the $3'$ region. The details of the interferometric mosaics are listed in Table 2, 3, and 4.

Calibration of the raw visibility was performed with the pipeline and manual reduction script for the cycle-5 data in Common Astronomy Software Applications (CASA v5.1.1-5). To recover the zero-spacing of the interferometric observations, we combined the 12 m, 7 m, and single dish data. The CASA (v5.4) tasks `tclean` and `feather` are used to deconvolve and merge the interferometric and single-dish maps. The automasking incorporated into `tclean` is applied to automatically mask regions during the cleaning process. The task `Mstrasform` is used to subtract the continuum emission. For observations of multiple fields, we clean and feather individual fields separately and combine individual fields to a single map. Weighted averages are applied in the overlapping area of adjacent fields. We used the Briggs robust parameter of 0.5. The image cubes were made at a velocity resolution of 2 km s^{-1} to enhance the signal to noise ratio. The native resolution of the CS(2-1), CS(3-2), CS(4-3), CS(5-4), and CS(7-6) are $1''$, $0.9''$, $1.3''$, $0.5''$,

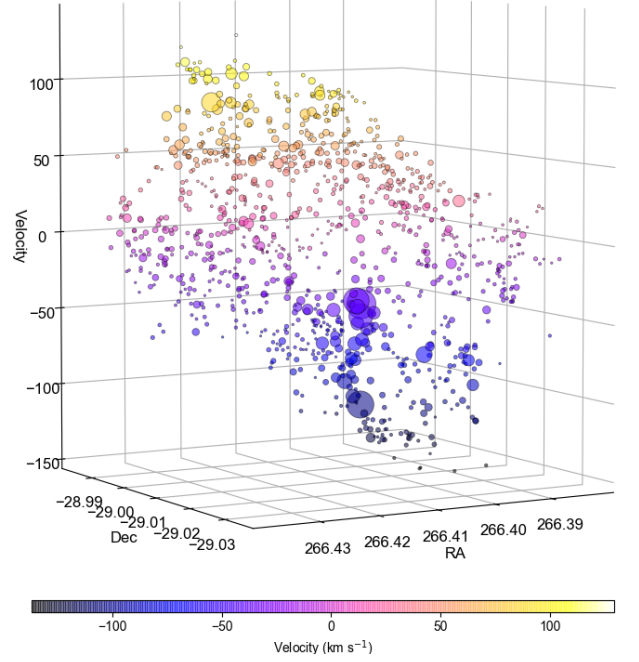


Figure 5. Position-position-velocity plot of the clumps. The color represents the centroid velocity and the sizes of circles are proportional to linewidth. All the properties are derived by Gaussian fitting.

and $0.8''$, respectively. For comparisons of all lines, we smoothed the maps to $1.3''$ ($= 0.05 \text{ pc}$), which is the lowest resolution of the CS(4-3) map, for further analysis. The noise level of the smoothed maps are 9.2, 10.8, 6.3, 32.4, $14.0 \text{ mJy beam}^{-1}$ for the CS(2-1), (3-2), (4-3), (5-4), and (7-6) maps, respectively.

3. RESULTS AND ANALYSIS

3.1. Integrated Intensity Maps

Figure 1 shows the integrated intensity maps of the CS(2-1), (3-2), (4-3), (5-4), and (7-6) lines, arising mostly from the CND and the surrounding streamers. A finding chart for the names of the features is presented in Figure 1. We follow the nomenclature of previously identified features in Christopher et al. (2005); Montero-Castaño et al. (2009); Martín et al. (2012). The CND and its surrounding streamers are more clearly disentangled from the foreground and background materials with the higher excitation transitions, which are much more reliable for studying the structure of the CND. Comparing our data with the previous SMA maps (Montero-Castaño et al. 2009; Liu et al. 2012; Martín et al. 2012), the improved spatial resolution of our ALMA maps by a factor of about 4 in linear scale and by more than a factor of 10 in area resolves a great detail of sub-structure

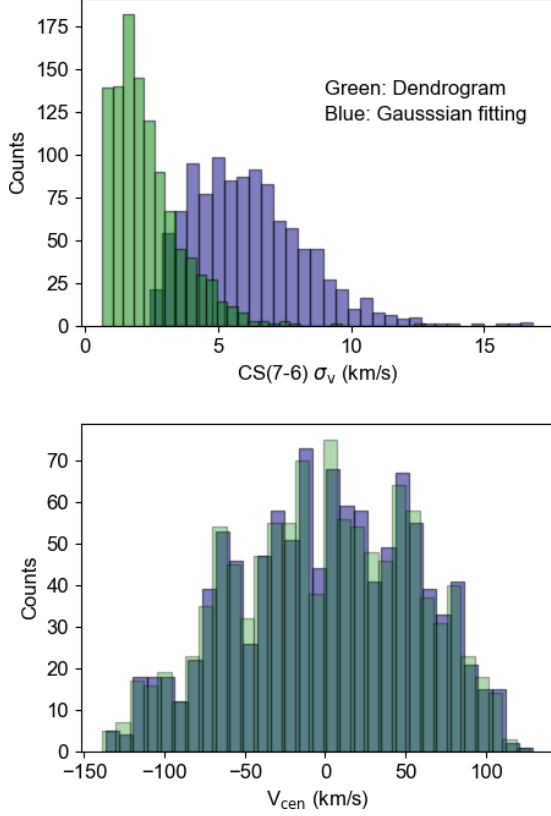


Figure 6. Histograms of the CS(7-6) σ_v and centroid velocity (V_{cen}) derived from *astrodendro* (green) and Gaussian fitting (blue). Dark green shows the overlapping area. The same clumps (number=1071) shown in Figure 3 are plotted here. Note that R_s is identical for the *astrodendro* and Gaussian approach as per definition. The linewidth of the Gaussian fits is larger due to underestimates by *astrodendro*, see discussion in text.

within the CND. Our maps show that the SMA 0.1 pc–0.25 pc sized clouds break into sub-parsec cores within the larger scale filaments. The CND no longer reveals itself as a complete ring but consists of multiple filaments wrapped around along the “ring”. The SW-lobe and western streamers are also resolved into multiple elongated filaments. The molecular clumps within the central 0.5 pc of Sgr A* are resolved into multiple filaments (Hsieh et al. 2019). The exquisite resolution in the ALMA maps displays a multitude of structures which lead to the impression that detailed dynamical features are now resolved and captured. Some areas show straight or clearly curved structures that appear to be tangential to rotation. We are likely also witnessing scale-dependent structures that are clearly organized with finer and finer sub-structures. A network of filaments, sub-filaments, and even thinner fibers is resolved. These finer networks are also not random, but appear to connect to main filaments and streamers. The CS(7-6)

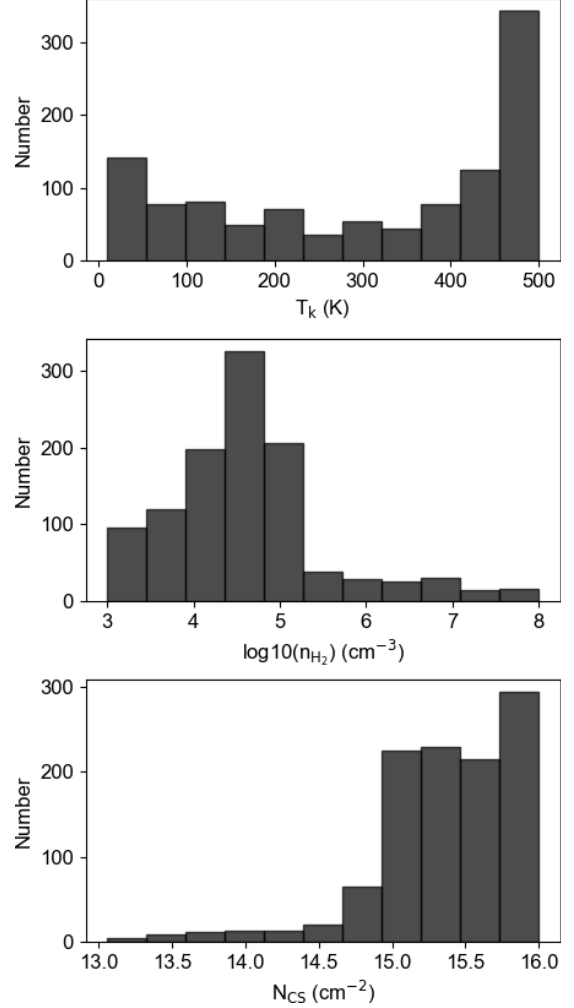


Figure 7. Histograms of the derived T_k , n_{H_2} , and N_{CS} in Radex.

channel maps are shown in Appendix (Figure 15). The detailed analysis of these structures and discussion of the channel maps will be presented in a forthcoming paper. In this paper we will focus on the compact components in this region.

3.2. CS Molecular Cloud Identification

3.2.1. Dendrogram

We identify molecular clumps with the CS data cubes using the Python package *astrodendro*, which decomposes emission into a hierarchy of structures in the position-position-velocity (PPV) cubes (Rosolowsky et al. 2008). The dendrogram decomposes the molecular structures into branches and leaves. Branches are structures that can be split into sub-structures called leaves, which have no further resolved substructure. The largest continuous structures surrounding the local maxima were categorized as trunks (i.e., no parent structures). We adopt parameters so that *astrodendro* iden-

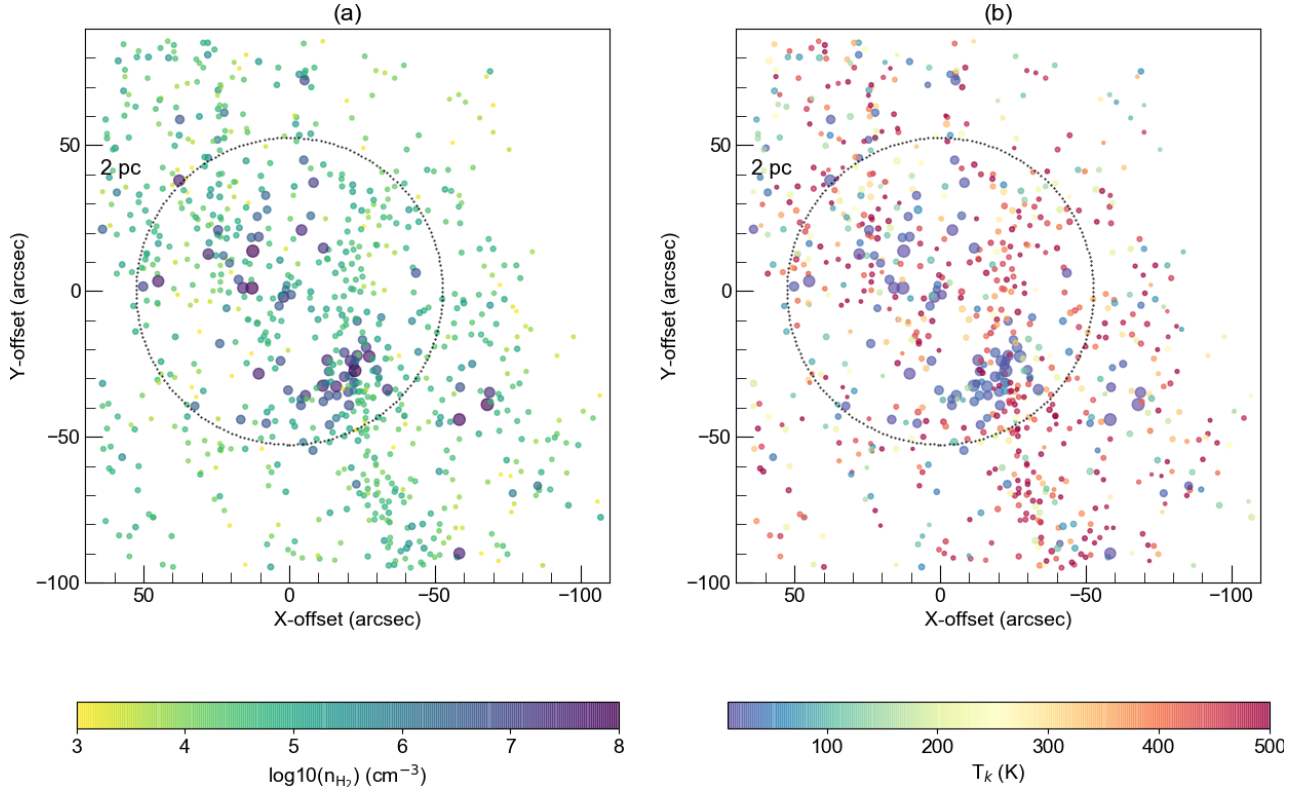


Figure 8. Clumps identified with *astrodendro* are shown in RA-Decl. offsets, centered on Sgr A*. (a) Colors represent the density of the cloud, sizes of the circles are also proportional to density. (b) Kinetic temperature in color. Sizes of circles are proportional to density, as in a). Radius of the dotted-circle is 2 pc.

tified local maxima in the cube above a threshold of $5 \sigma_{\text{rms}}$, and at least $2.5 \sigma_{\text{rms}}$ above the merging level of the branches with adjacent structures. In addition to the intensity threshold for decomposition, we also specify the minimum number of pixels that a structure should span to be the area of one synthesized beam, and remove the clumps with linewidths smaller than 2 km s^{-1} .

The primary goal is to decompose spectroscopic components superimposed along the line of sight in this complicated region. Since the high excitation line is expected to be less biased by the foreground emission, to cleanly identify the “leaves” associated with the CND and streamers, we identify clumps with the CS(7-6) data. The numbers of the leaves (hereafter clumps) identified by *astrodendro* are 2379. The basic properties of the identified clumps are calculated by *astrodendro*. The root-mean-square (rms) size of the major and minor axes of clumps (σ_{maj} , σ_{min}), and the rms linewidth (σ_{vden}) are determined by the moment calculations. The calculations of moments are based on pixels assuming that the cloud is continuous and bordered by an isosurface of a certain brightness temperature. The position and velocity of the clumps are determined by the intensity-

weighted centroids of pixels within a cloud. The sizes of the clumps (σ_r) are defined by the geometric mean of σ_{maj} and σ_{min} ($\sigma_r = \sqrt{\sigma_{\text{maj}} \sigma_{\text{min}}}$). Multiplying σ_r with a coefficient 1.91 converts the rms size to the effective spherical radius of the cloud (R_s) (Solomon et al. 1987; Bertoldi & McKee 1992). The histograms of these basic properties are shown in Figure 2.

We use a bootstrap approach to calculate the uncertainties in the derived properties (Rosolowsky & Leroy 2006). For each cloud, we generate a trial cloud and measure its properties (σ_{maj} , σ_{min} , σ_v) by random sampling pixels (allowed repetition) within the boundaries of the cloud in position and velocity space. We repeat this process 500 times and use the median absolute deviation to estimate an rms uncertainty for each property. The uncertainty is scaled by the square root of the number of pixels of the synthesized beam to account for the oversampling rate.

3.2.2. Gaussian Fitting

To measure the total flux of every transition in a homogeneous area and position, using the centroid positions and velocities of clumps identified in the CS(7-6) cube, we extract spectra from the cube averaged over

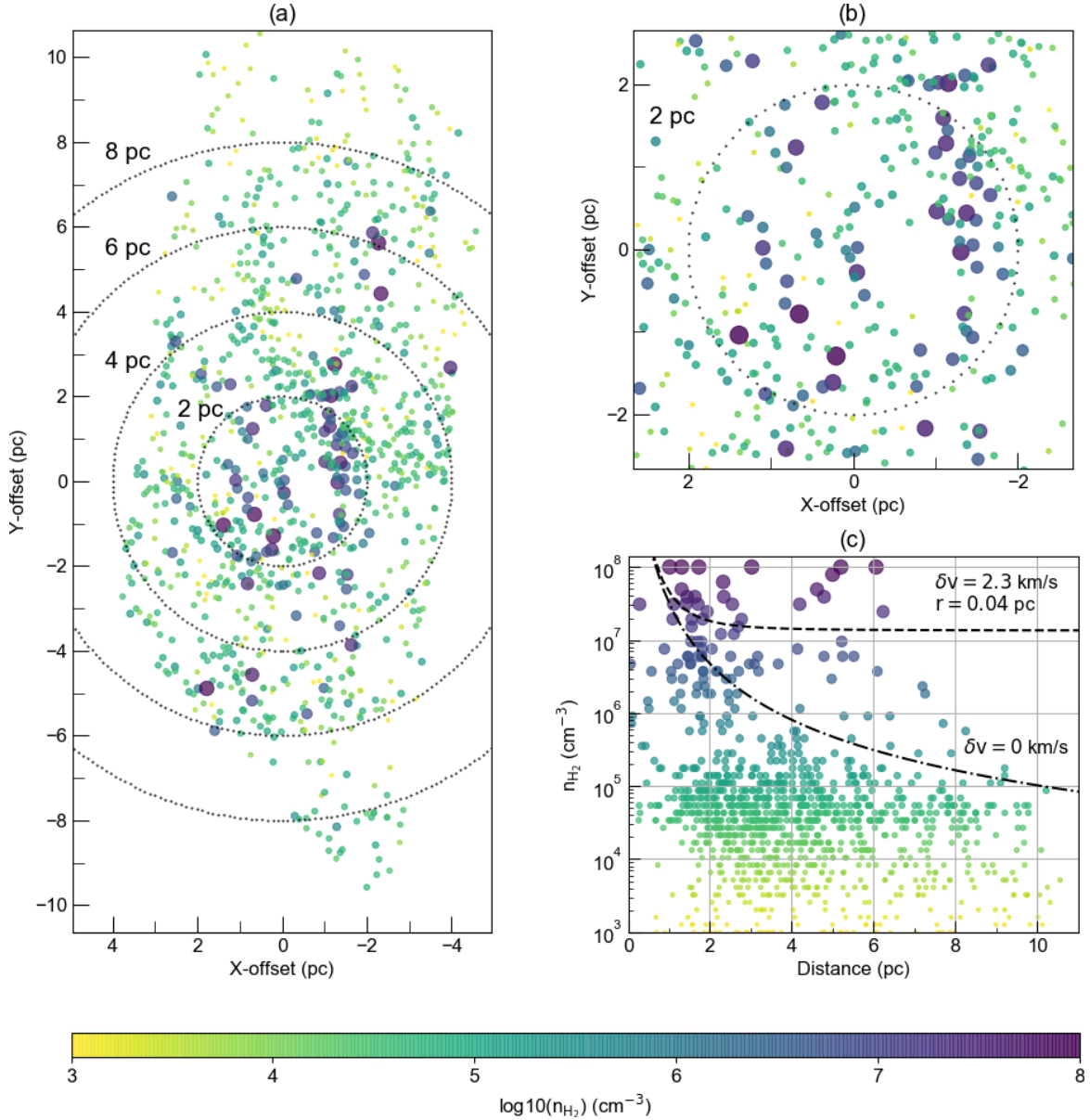


Figure 9. Density of clumps as a function of the deprojected distance from Sgr A*. Color represents n_{H_2} in logarithmic scale and the circle sizes are proportional to n_{H_2} . Dotted circles mark the galactocentric distance of 2 to 8 pc. (a) Clump distribution in the deprojected space for the full range. (b) Same as (a), but for the central ± 2 pc. (c) n_{H_2} of clumps are shown as a function of the deprojected distance from Sgr A*. The minimum density for tidal stability ($n_{\text{crit}0}$) is labeled with the dot-dashed curve. The critical density (n_{crit}) for gravitational collapse is labeled with the dashed curve for a cloud with a mean R_s of 0.04 pc and a mean velocity dispersion of 2.3 km s^{-1} .

the σ_{maj} and σ_{min} , and fit a single Gaussian profile to every CS transition. Single Gaussian is in general a good approximation of the clumps. The fitted intensity peaks and linewidths are then used to calculate the flux for analysis of radiative transfer modeling (next section). We have selected clumps where all transitions simultaneously show a fitting result higher than 3σ . However, we find that including CS(2-1) leads to fewer clumps passing the filter of 3σ (748 clumps). To improve the statistical results, we exclude CS(2-1). We also exclude

the clumps with a difference of linewidths larger than 5 km s^{-1} , which is a 2.5σ limit of the velocity resolution. The resulting number of clumps is 1071, which accounts for 54% of the CS flux of the 2379 clumps. The histograms of the effective spherical radius ($R_s = \sigma_r \times 1.91$), the rms linewidth of the CS(7-6) (σ_{vfit}), and the central velocity derived from Gaussian fitting are shown in Figure 3. The size-linewidth relation of these 1071 clumps is shown in Figure 4. We also present the cloud properties in PPV space in Figure 5. It is clearly seen that

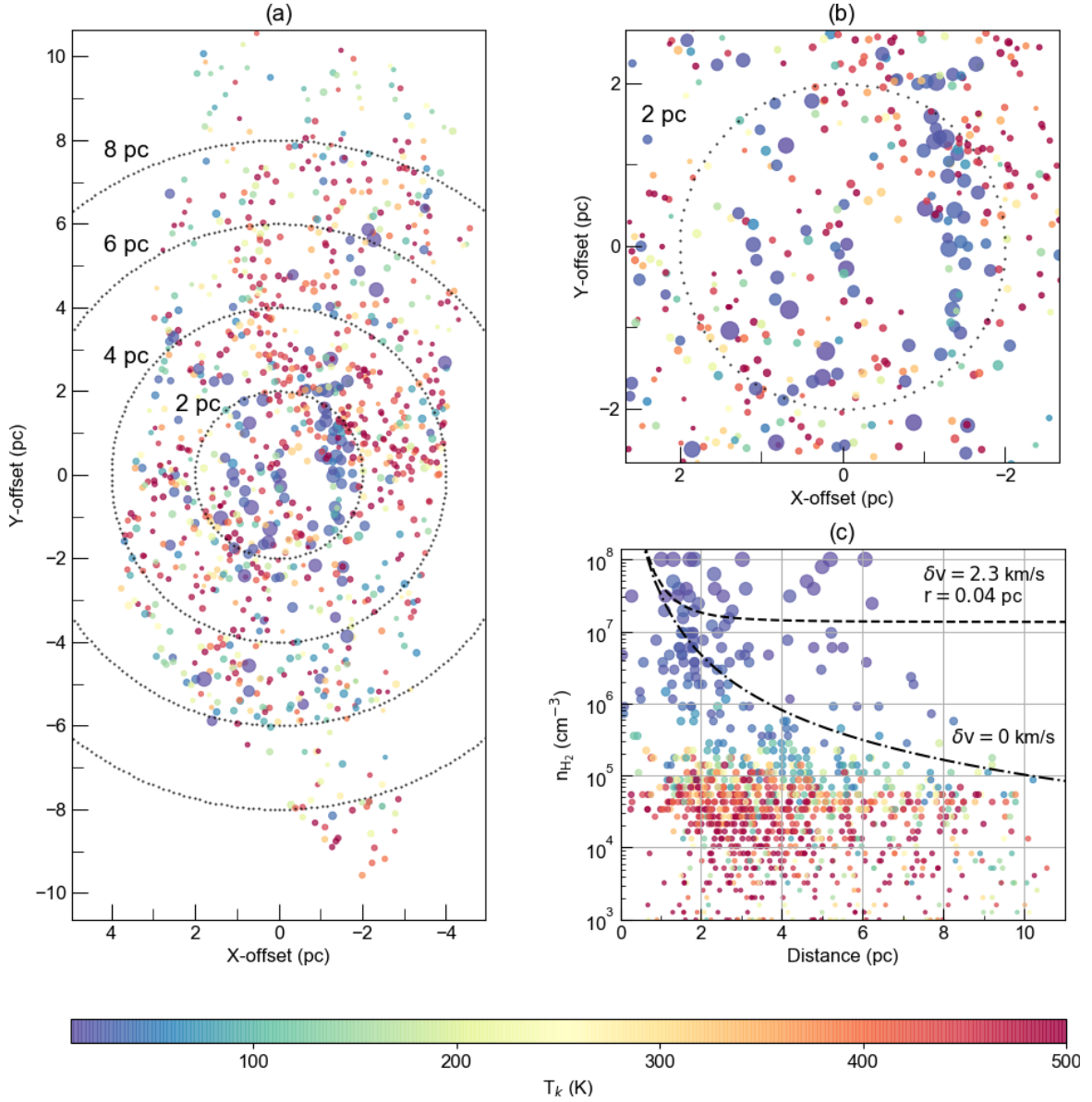


Figure 10. As in Figure 9, but color represents T_k .

the clumps in the southern/northern part of the CND (blue/red shifted velocities), and within the streamers have broader linewidths than the surrounding gas.

Comparisons of the velocity dispersion and centroid velocity given by *astrodendro* and our Gaussian fitting are shown in Figure 6. The centroid velocities are consistent with each other. Note that in *astrodendro*, the σ_r of a leaf is defined by the high isocontour levels (bijection method). This leads to an underestimated σ_v because the spectral profile is truncated by the isosurface boundary (Rosolowsky & Leroy 2006). This effect can be seen in Figure 6. The σ_v given by the *astrodendro* is smaller than our Gaussian fitting (at the same position). Also note that we do not correct for the resolution effect, this is because a simple deconvolution of the clump size esti-

mated by the bijection method may be underestimated, as discussed in Rosolowsky & Leroy (2006).

3.3. Statistical Equilibrium and Non-LTE Radiative Transfer

We use the radiative transfer code Radex (van der Tak et al. 2007) to derive the physical properties of the molecular gas in the CND and its surrounding. Radex performs the statistical equilibrium calculations and uses the escape probability formalism (Goldreich & Kwan 1974) to solve the statistical equilibrium equations to model the observed line intensities for given physical conditions. The statistical equilibrium calculations account for the opacity effects as well as subthermal excitation.

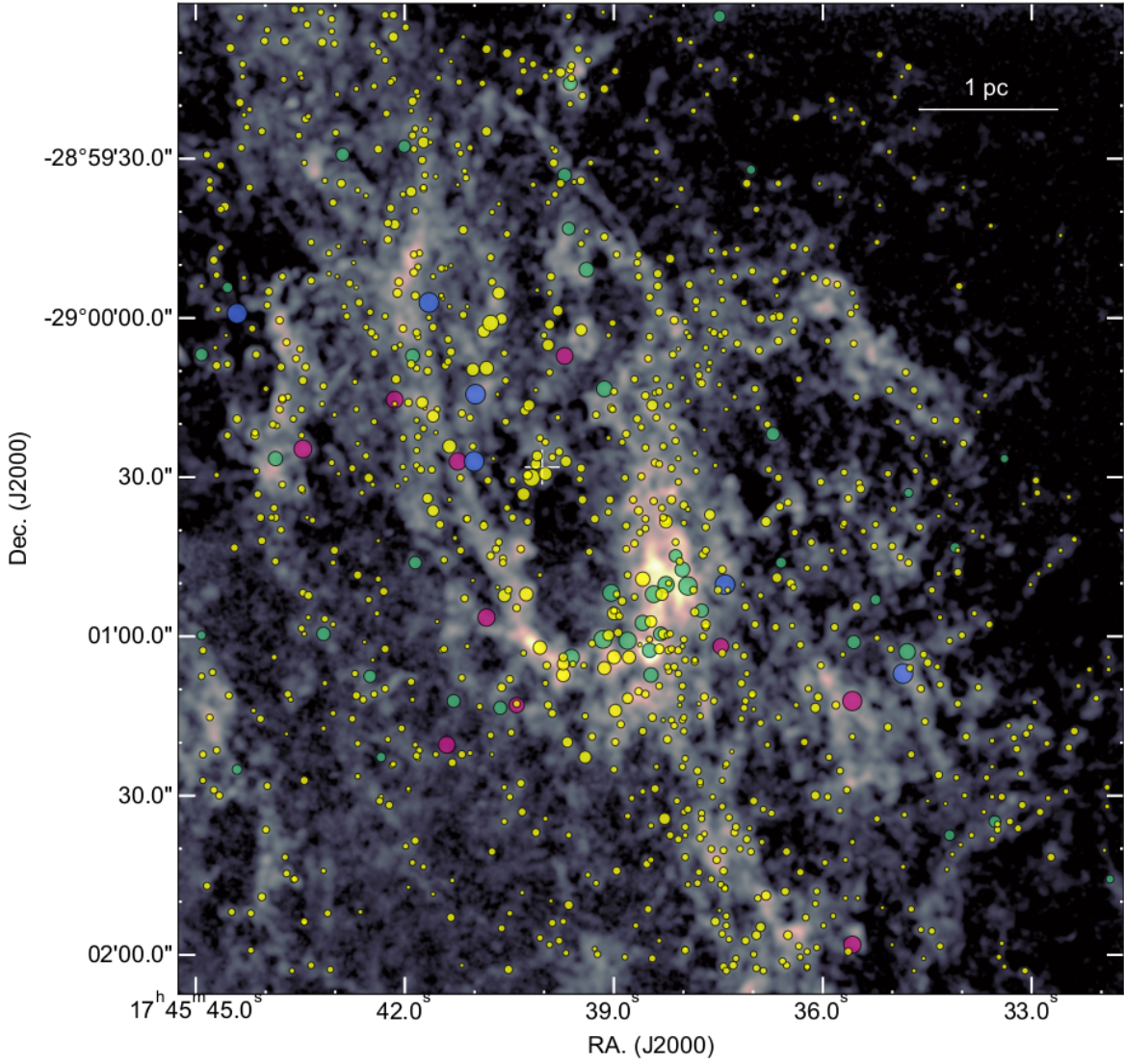


Figure 11. Clumps overlaid on the moment 0 map of the CS(7-6) line. Yellow circles are clumps below $n_{\text{crit}0}$ and will be dispersed by tidal force. Green circles are stable clumps within $n_{\text{crit}0}$ and n_{crit} and will neither be dispersed by tidal force nor collapse by gravity. Red and blue circles are clumps above n_{crit} and able to collapse to form stars: the blue clumps correspond to the upper limit ($\leq 10^8 \text{ cm}^{-3}$). The circle sizes are proportional to n_{H_2} .

The general solution of the radiative transfer equation for a homogeneous medium is,

$$I_\nu = B_\nu(T_{\text{ex}})(1 - e^{-\tau_\nu}) + I_\nu^{\text{bg}}e^{-\tau_\nu}, \quad (1)$$

where I_ν is the specific intensity and I_ν^{bg} is the background emission at line frequency ν , in units of $\text{erg s}^{-1} \text{ cm}^{-2} \text{ Hz}^{-1} \text{ sr}^{-1}$. T_{ex} and τ_ν are the excitation temperature and the optical depth, respectively. $B_\nu(T)$ is the blackbody radiation field at temperature T . The intensity of the line subtracting the background emission ($I_\nu - I_\nu^{\text{bg}}$) is calculated for each molecule with varying molecular column density, H_2 density of the main collision partner, and kinetic temperature. Note that the Rayleigh-Jeans approximation is generally not valid for molecular line emission at submm wavelengths of ther-

mal emission. We thus calculate I_ν and do not use the Rayleigh-Jeans temperature calculated by the code. In this paper, we use the uniform sphere geometry, a single collision partner (H_2), and a background temperature of 2.73 K. The collisional rate and spectroscopic data of the CS molecule were taken from Leiden Atomic and Molecular Database (LAMDA) (Schöier et al. 2005; Lique et al. 2006).

We construct a $50 \times 50 \times 50$ grid of parameter space for kinetic temperature (T_K), molecular hydrogen density (n_{H_2}), and column density of CS molecule (N_{CS}).

1. T_K is from 10 K to 500 K.
2. n_{H_2} is from 10^3 cm^{-3} to 10^8 cm^{-3} .

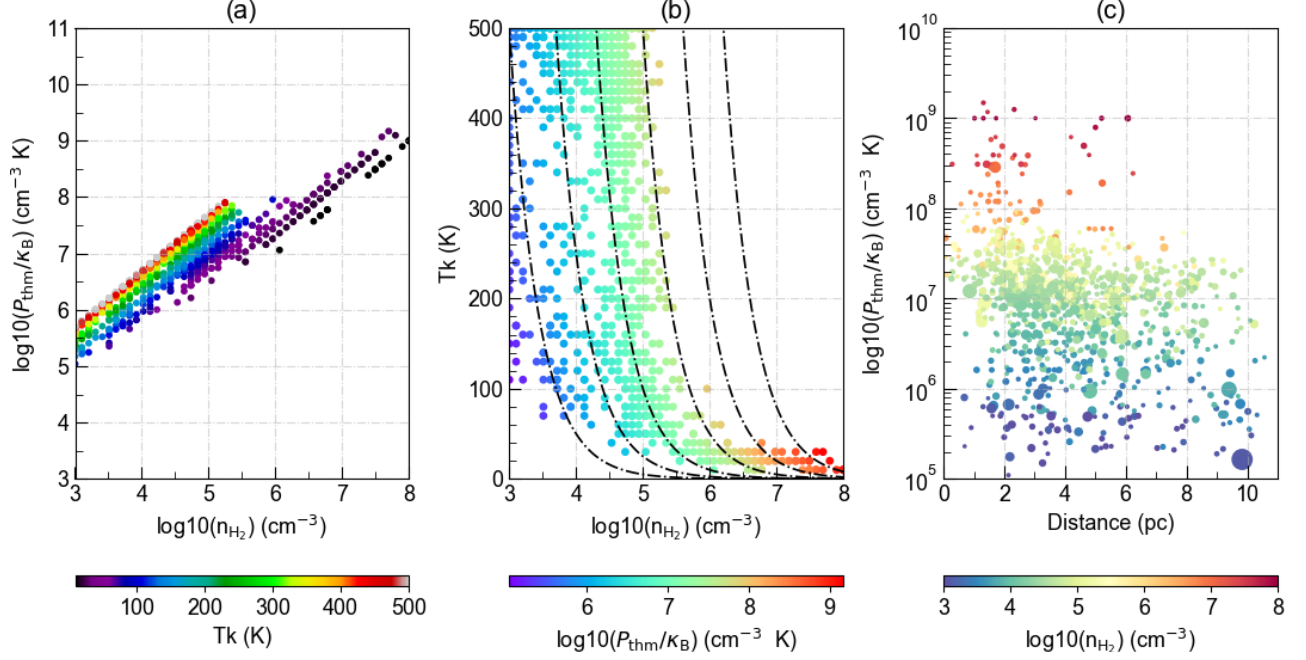


Figure 12. (a) Thermal pressure of clumps P_{thm}/k_B (cm⁻³ K) vs. n_{H_2} . Color denotes T_k . The high density clumps ($\geq 10^6$ cm⁻³) do not have high temperature components as shown in the lower density clumps. (b) T_k vs. n_{H_2} . Colors indicates P_{thm}/k_B . Isobaric curves of $P_{\text{thm}}/k_B = 5 \times 10^5, 2.5 \times 10^6, 1 \times 10^7, 5 \times 10^7, 2 \times 10^8, \text{ and } 8 \times 10^8$ cm⁻³ K are labeled with the dot-dashed curves. (c) P_{thm}/k_B vs. the distance from Sgr A* with color indicating n_{H_2} . The circle size is proportional to R_s , showing that higher density clumps have smaller size.

3. N_{CS} is from 10^{12} cm⁻² to 10^{16} cm⁻².

We then derive the best-fit T_K , n_{H_2} , and N_{CS} by comparison with the velocity integrated intensities (line flux) $\int I_\nu dv = 1.0645 I_\nu \Delta v$, where Δv is the full width half maximum (FWHM) of the line, and the factor of 1.0645 is a correction from the adopted square line profile in Radex to Gaussian profile. I_ν is derived by Equation 1. The model integrated intensity is conserved at each specific condition. The same amount of radiation is spread over the spectral profile, and therefore I_ν (also called line intensity peak in observation), depends on linewidth because the opacity changes. The opacity tends to be lower with broader linewidths because the same amount of radiation is spread over wider velocities. The variation of opacity as a function of linewidth is not linear, especially in higher density conditions. We therefore generate the Radex models by incrementing Δv with 5 km s⁻¹ intervals from 5 km s⁻¹ to 40 km s⁻¹, and fit the data at corresponding intervals. The comparison of the models and the observed four transitions (excluding CS(2-1)) is performed with the χ^2 -statistics for each set of parameters. We find the best fit models by minimizing χ^2 value.

The brightness unit measured in the radio map is often defined in Jy per beam (Jy/beam) which is the same dimension as specific intensity (erg s⁻¹ cm⁻² Hz⁻¹ beam⁻¹) but averaged over the Gaussian beam (synthe-

sized beam). Therefore, to compare with the model, we need Jy beam⁻¹ to be a more physical unit of per steradian. We divide by the solid angle of the beam in steradian (Ω_{beam}).

$$\langle I_\nu \rangle (\text{Jy sr}^{-1}) = \frac{I_\nu (\text{Jy beam}^{-1})}{\Omega_{\text{beam}}}, \quad (2)$$

$$\Omega_{\text{beam}} = \frac{\pi \theta_{b1} \theta_{b2}}{4 \ln 2} \left(\frac{\pi}{180^\circ \times 3600} \right)^2, \quad (3)$$

where θ_{b1} and θ_{b2} are the gaussian major and minor axis of the synthesized beam in units of arcsec.

However, several uncertainties arise for unknown source sizes and non-uniform structures. With an insufficient resolution, it is not possible to avoid these uncertainties. For unresolved sources (compact sources or point sources), the values in Jy/beam are equal to the flux density (Jy) because the total fluxes are covered within one beam. Therefore, to calculate the specific intensity from flux density, we should divide the measured value ($I_{\nu, \text{map}}$) by the solid angle of source sizes (Ω_{source}). Sources smaller than half of the synthesized beam are almost indistinguishable and the accuracy is less than 10%. Therefore, for such sources a lower limit is given from dividing by the beam size, because the source sizes are unknown. If the sources are resolved, the assumption is that sources have a uniform intensity distribution. To

optimize the comparison with the model, we introduce a scaling factor in the fitting to correct for the uncertainty of intensity from the above reasons. This is similar to a beam filling factor but not exactly the same because we do not use a temperature scale. The best fitted scaling factors are between 0.05 to 2.5.

Histograms of the derived T_k , n_{H_2} , and N_{CS} from the Radex analysis are shown in Figure 7. The majority of the clumps have $T_k \geq 400$ K, and show a smooth distribution between 50 K to 400 K. Gas with $n_{H_2} \leq 10^5 \text{ cm}^{-3}$ dominates the region. Overall, 78% of the compact clumps in this region have $T_k \geq 50$ K and $n_{H_2} \leq 10^5 \text{ cm}^{-3}$. High temperature and low density environments in the CNL were reported in previous studies using single-dish data. Bradford et al. (2005), derived warm 200-300 K and moderate densities $5\text{--}7 \times 10^4$ with CO(7-6). Oka et al. (2011) reported $T_k = 63$ K and $n_{H_2} = 10^4 \text{ cm}^{-3}$ with CO(1-0) and CO(3-2). Requena-Torres et al. (2012) constrained the temperatures of the southwest lobe of the CNL to $T_k = 200$, $n_{H_2} = 10^{4.5} \text{ cm}^{-3}$ for a low excitation component, and $T_k = 500$, $n_{H_2} = 10^{5.2} \text{ cm}^{-3}$ for a high excitation component with the nine CO transitions. Using the HCN(3-2), (4-3), and (8-7) lines, Mills et al. (2013) showed that the southern CNL has $T_k = 94 - 171$ K and $n_{H_2} = 10^{5.9-6.5} \text{ cm}^{-3}$, and the northern CNL has $T_k = 270$ K and $n_{H_2} = 10^{5.6} \text{ cm}^{-3}$. Harada et al. (2015) derived the $n_{H_2} = 7.26 \times 10^5 \text{ cm}^{-3}$ and $N_{CS} = 1.07 \times 10^{15} \text{ cm}^{-2}$ with the CS(2-1), (6-5), (7-6), (8-7) lines in the southern lobe of the CNL. It appears that with the CS and HCN lines, higher densities are determined than CO. With the high resolution ALMA data, we further reveal the existence of cooler and denser components with $T_k \leq 50$, $n_{H_2} = 10^{6-8} \text{ cm}^{-3}$ at sub-pc scale. In conclusion, the CNL consists of a mixture of warm ($T_k \geq 50 - 500$ K, $n_{H_2} = 10^{3-5} \text{ cm}^{-3}$) and cold gas ($T_k \leq 50$ K, $n_{H_2} = 10^{6-8} \text{ cm}^{-3}$) (Herrnstein & Ho 2005).

4. DISCUSSION

In Figure 8 we show the spatial distribution of the n_{H_2} and T_k derived from the Radex model on the projected sky. The ALMA high resolution data reveal a broad distribution of densities and temperatures at sub-pc scale associated with the CNL and the surrounding streamers. In addition, these features contain numerous compact dense cores with sizes of ≤ 0.05 pc in the ALMA maps. A key question is whether these dense cores can survive the tidal disruption near Sgr A*. With the high resolution ALMA map, we will derive the cloud properties at sub-pc scale.

4.1. Stability of Clumps as a Function of Distance from Sgr A*

To compare the gas densities with the tidal limit – the minimum density for tidal stability, as a function of distance from Sgr A*, we deproject the distances of clumps with respect to Sgr A*. The inclination and position angle used for deprojection are 70° and 30° , respectively. The inclination of 70° is the median between the 65° to 80° of the streamers and the CNL (Martín et al. 2012; Hsieh et al. 2017). The spatial distributions of densities and temperatures of clumps in the deprojected plane are shown in Figure 9(a), (b) and figure 10(a), (b), respectively. In the deprojected map, the radii of 2, 4, 6, and 8 pc are shown as dotted circles. The CNL is located mostly between 2 to 3 pc, while the streamers are located between 2 to 8 pc. This deprojection assumes that the structures are aligned in the same plane (cf. Hsieh et al. 2019). We find that there is no clear trend or correlation of the n_{H_2} and T_k as a function of the distance from Sgr A*. Our results appear consistent with the previous studies by Christopher et al. (2005), who derived core densities at a scale of 0.25 pc and reported that there is no correlation between n_{H_2} and the distance from Sgr A*.

To find the critical density for disruption by tidal shear due to Sgr A* and the nuclear star clusters, we use the model from Vollmer & Duschl (2000), for the enclosed mass

$$M_{\text{total}} = M_{\text{BH}} + 1.6 \times 10^6 r_{\text{pc}}^{1.25} M_{\odot}, \quad (4)$$

where $M_{\text{BH}} = 4 \times 10^6 M_{\odot}$ is the mass of Sgr A* (Ghez et al. 2005) and r_{pc} is the radial distance from Sgr A* in units of pc. The tidal force at the position x from the cloud center located at r is given by

$$\begin{aligned} T(x) &= -x \frac{d}{dr} \left(\frac{GM_{\text{total}}}{r^2} \right) \\ &= x \frac{GM_{\text{BH}}}{(1\text{pc})^3} (2r_{\text{pc}}^{-3} + 0.3r_{\text{pc}}^{-1.75}) \\ &= x\mathcal{T}_0(r), \end{aligned} \quad (5)$$

where $\mathcal{T}_0 = 2GM_{\text{BH}}r^{-3}(1 + 0.15r_{\text{pc}}^{1.25})$. For a cloud with mass M and radius $R (= R_s)$, tidal disruption occurs if

$$\frac{GM}{R^2} < R\mathcal{T}_0(r). \quad (6)$$

Assuming the cloud is uniform, its mass is given by

$$M = 1.36m_{H_2}n_{H_2} \left(\frac{4\pi R^3}{3} \right), \quad (7)$$

where 1.36 is a correction for He and other elements, and m_{H_2} is the molecular hydrogen mass. Assuming that the

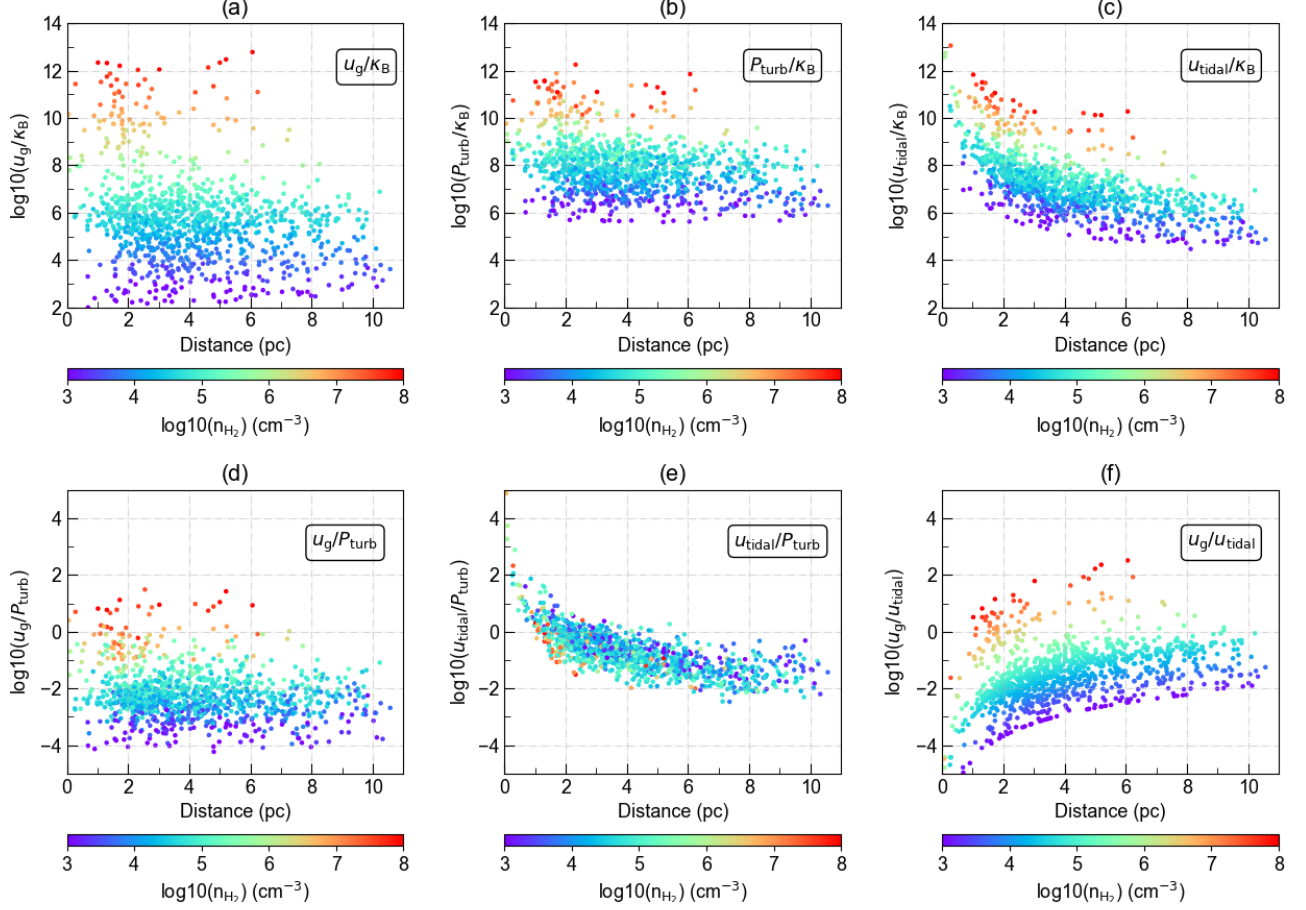


Figure 13. (a) Gravitational energy density u_g , (b) turbulence pressure P_{turb} , and (c) energy density of tidal force (u_{tidal}) as a function of the galactocentric distance from Sgr A*. Ratios among two energy components are displayed in the lower panels.

cloud has uniform density, the critical density ($n_{\text{crit}0}$) of molecular hydrogen against tidal force is then given by

$$n_{\text{crit}0} = 2.8 \times 10^7 \left(r_{\text{pc}}^{-3} + 0.15 r_{\text{pc}}^{-1.75} \right) \text{ cm}^{-3}, \quad (8)$$

which is the tidal limit. In Figures 9(c) and 10(c), we plot $n_{\text{crit}0}$ as a dot-dashed line. Clumps above this line are tidally stable. A vast majority of the high temperature clumps (with $T_k \geq 50$ K) have densities smaller than $n_{\text{crit}0}$ in the central 10 pc of the GC. The cooler components (with $T_k \leq 50$ K) have in general higher density than the $n_{\text{crit}0}$. We also find that within the central 1 pc, none of the clumps are above $n_{\text{crit}0}$.

4.2. Effects of Turbulence

The above analysis does not take into account the effects of internal and external pressures on the cloud stability. In the presence of the external force \mathbf{F}_{ext} , the scalar virial theorem in the equilibrium state for an unmagnetized gas reads

$$0 = 2U + W - P_{\text{ext}} \int_S \mathbf{x} \cdot d\mathbf{A} + \int_V \rho \mathbf{x} \cdot \mathbf{F}_{\text{ext}} d^3x, \quad (9)$$

where U is the internal energy, $W = -3GM^2/(5R)$ is the gravitational potential energy, P_{ext} is the pressure of an external medium, and $F_{\text{ext}} = T(x)$ is the (external) tidal force. Assuming that the turbulent pressure dominates the thermal pressure inside the cloud, Equation (9) becomes

$$0 = 3M\sigma_v^2 - \frac{3GM^2}{5R} - 4\pi R^3 P_{\text{ext}} + \frac{3}{5} \mathcal{T}_0 M R^2, \quad (10)$$

where M is the cloud mass, $R = R_s$, σ_v is the velocity dispersion, and P_{ext} is the external pressure. Self-gravity and external pressure tend to confine the cloud against the internal turbulence and tidal force tending to disperse the cloud.

For a time being, we assume $P_{\text{ext}} = 0$ (we will discuss the effect of P_{ext} in the later section). Then, Equation (10) gives

$$n_{\text{crit}} = 2.8 \times 10^7 \left(r_{\text{pc}}^{-3} + 0.15 r_{\text{pc}}^{-1.75} \right) \text{ cm}^{-3} + 4.1 \times 10^7 \left(\frac{\sigma_v}{10 \text{ km s}^{-1}} \right)^2 \left(\frac{R}{0.1 \text{ pc}} \right)^{-2} \text{ cm}^{-3}, \quad (11)$$

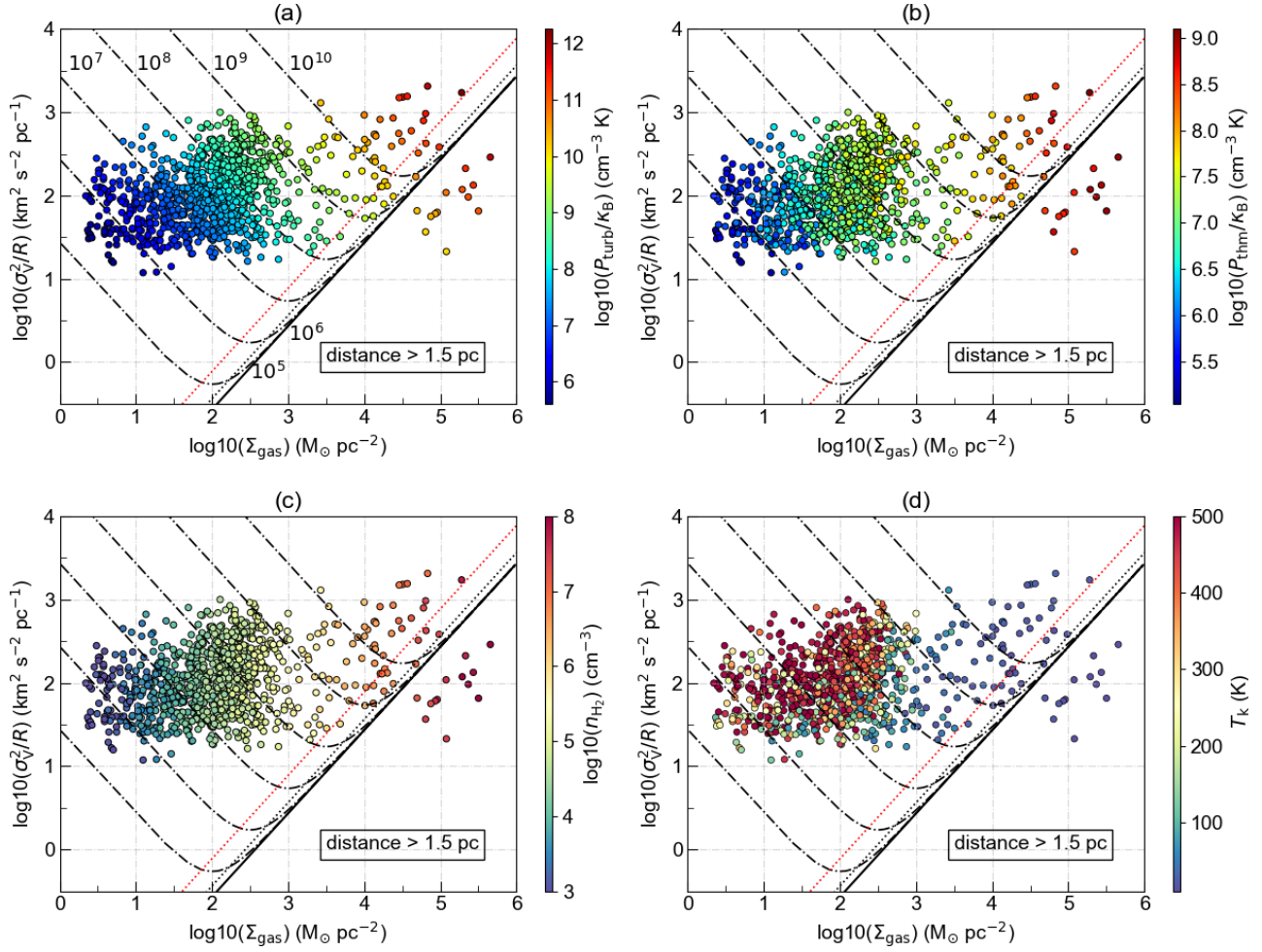


Figure 14. (a) Distribution of the clumps in the $\sigma_v^2/R - \Sigma_{\text{gas}}$ plane. The identified clumps (at distance from Sgr A* > 1.5 pc) are overlaid colored by their turbulent pressure. The dot-dashed curves draw Equation (16) with varying external pressure ($P_{\text{ext}}/k_B = 10^5 - 9 \text{ cm}^{-3} \text{K}$), ignoring magnetic fields and tidal force. The solid straight line is the solution with $P_{\text{ext}} = 0$. The black and red dotted lines (corresponding to critical configurations) show the location of critical mass of clumps determined from the assumptions of constant density (Equations 2 and 3 in Field et al. 2011) and centrally concentrated internal density structure (Equations 4 and 5 in Field et al. 2011), respectively. Clumps above the dot-dashed lines at corresponding P_{ext} and σ_v^2/R are gravitationally unstable. (b), (c), (d) Same as (a) but colored by thermal pressure P_{thm} , n_{H_2} , T_k , respectively.

which is the critical density including tidal force and turbulence. This is identical to Equation (8) if $\sigma_v = 0$. Using the results of *astrodendro*, we overlay n_{crit} (dashed line) using the mean values of $\sigma_v = 2.3 \text{ km s}^{-1}$ and $R_s = 0.04 \text{ pc}$ in Figures 9(c) and 10(c). Here we plot all the clumps. Figure 16 in Appendix plots in the density-distance plane the clumps with uncertainties of densities less than 1 order of magnitude. The critical densities n_{crit} and n_{crit0} define 3 different regimes.

1. Clumps below n_{crit0} are tidally disrupted and will disperse.
2. The clumps that fall in between n_{crit0} and n_{crit} are tidally stable and at the same time supported by turbulence against gravitational collapse. Col-

lapse is still not happening and with growing dispersion these clumps could also disperse.

3. The clumps above n_{crit} are tidally stable and have densities large enough that they can collapse. The free-fall time is roughly a few thousand years (see Figure 17 in Appendix).

Note that the curve derived by the mean values of σ_v and R_s only presents an overall threshold of n_{crit} . The classification of clumps in the 3 different regimes based on the individual value of the clump is presented in Figure 11. The fractions of gas mass and number in each type are presented in Table 5. At the distance from Sgr A* > 1.5 pc, the internal energy (turbulence) is more important than the tidal force, and supports clumps against gravity. However, within the central 1.5 pc, tidal force

overrides again and the threshold densities for gravitational collapse quickly rises to $\geq 10^8 \text{ cm}^{-3}$.

Clumps below $n_{\text{crit}0}$ account for $16_{-7.5}^{+28} \%$ of the total mass in our samples ($2.5_{-0.4}^{+1.0} \times 10^4 M_{\odot}$). Note that this mass is a lower limit. 94% of the clumps (by numbers) belong to this regime, suggesting that most of the clumps are tidally unstable. Among the clumps we identified, nearly $84_{-37}^{+16} \%$ of the total gas mass is tidally stable ($28_{-12}^{+24} \%$ of the total mass is gravitationally stable and $56_{-28}^{+22} \%$ of the total mass is gravitationally unstable). The 16 seemingly gravitationally unstable clumps are listed in Table 6. The 36.2 GHz and 44.1 GHz class I methanol masers were observed in the CND (Yusef-Zadeh et al. 2008; Sjouwerman et al. 2010; Pihlström et al. 2011). The class I methanol masers are collisionally pumped and are associated with shocked gas or outflows, which could be a signature of early phase of star formation (cf. Yusef-Zadeh et al. 2008, 2015). However, there is no $850\mu\text{m}$ continuum emission detected in association with these masers, and no HCN gas associated with corresponding velocities (e.g. Liu et al. 2013). These masers were suggested to be produced by the shock during cloud-cloud interactions (Sjouwerman et al. 2010). It has not yet been concluded that a star is about to form in the CND or the star formation is quenched. If the star formation is quenched in the CND, additional forces such as internal magnetic pressure/tension, rotational shear, or cloud rotation (Vollmer & Duschl 2000) may exist to support the clouds against collapse.

4.3. Thermal and Non-thermal Properties of the Clouds

We calculate the thermal pressure (P_{thm}) of the clumps with the derived gas density and kinetic temperature as

$$P_{\text{thm}}/k_B = n_{\text{H}_2} T_k, \quad (12)$$

where k_B is the Boltzmann constant. The relations between $P_{\text{thm}} - n_{\text{H}_2}$ and $T_k - n_{\text{H}_2}$ are shown in Figure 12. The $P_{\text{thm}} - n_{\text{H}_2}$ relation resembles a typical phase diagram for diffuse ISM and has a break at $n_{\text{H}_2, \text{crit}} = 3 \times 10^5 \text{ cm}^{-3}$, such that high density clumps with $n_{\text{H}_2} > n_{\text{H}_2, \text{crit}}$ are cold with $T_k < 50 \text{ K}$, while low density clumps with $n_{\text{H}_2} < n_{\text{H}_2, \text{crit}}$ are relatively warm with $T_k > 50 \text{ K}$. Thermal pressure of low density clumps varies by an order of magnitude for fixed n_{H_2} . Figure 12(b) shows that the temperature monotonically decreases as the density increases, implying that pressure varies a lot from cloud to cloud. Figure 12(c) hints that the pressure of clumps is overall systematically growing towards Sgr A*, i.e., the highest pressure clumps are found nearest to Sgr A*, while lower-pressure clumps are at larger distances.

Interestingly, we find that there is no high density cloud with high temperature. If high density clumps are able to form stars, the lack of high temperature gas may hint an maximum mass of newly-forming stars because the Jeans mass is proportional to $T^{3/2}$. It is possible that the CS transitions we observed are not sensitive to high temperature and high density gas, and we need to observe the mid-infrared high-J lines to probe these missing populations. However, since the cooling rate is proportional to the square of gas density, and if the dust-gas coupling is better toward high density clouds, the cooling can be efficient (Krumholz 2011).

We further calculate the energy densities of turbulence, tidal force, and gravity to compare their relative importance acting on the clumps. The gravitational energy density is given by

$$u_g = \frac{9}{20\pi} \frac{GM^2}{R^4}. \quad (13)$$

The turbulence energy density is

$$P_{\text{turb}} = \frac{3}{2} \rho \sigma_v^2, \quad (14)$$

where ρ is the mass density of gas and σ_v is from *astro-dendro*. The energy density of the tidal force is given by

$$u_{\text{tidal}} = \frac{9}{20\pi} \frac{\mathcal{T}_0 M}{R}. \quad (15)$$

Figure 13 plots the energy densities and their ratios. In contrast to u_{tidal} , which is a decreasing function of r , we find that u_g and P_{turb} do not change much with r , although there is a growing number of clumps with an increased level of turbulence closer to Sgr A*. This is similar to the trend seen in the thermal pressure.

Figure 13 shows that for most clumps, $P_{\text{turb}} > u_{\text{tidal}} > u_g$ at $r > 2 \text{ pc}$ except for the densest clumps. In what follows, we ignore u_{tidal} in comparison with P_{turb} . We note that although the clumps are warmer in the GC, turbulence is still more important than the thermal energy. The ratio $u_{\text{tidal}}/P_{\text{turb}}$ depends on the galactocentric distance, but independent of the cloud density. Therefore, the relative importance of each term is dependent on the mass of the black hole and turbulence. We note that the tidal force can fully override turbulence for a black hole mass 100 times larger than Sgr A*. The physical condition and distribution of energy in external galaxies can be largely different from Sgr A*.

4.4. Can External Pressure Stabilize Clouds?

To study the role of the external pressure (P_{ext}) on confining molecular clouds, we compare our data with the model presented by Field et al. (2011). In their model, a non-magnetized virial theorem immersed in

a uniform external pressure is applied. The pressure-bounded virial equilibrium (PVE) requires

$$\frac{\sigma_v^2}{R} = \frac{1}{3} \left(\pi \Gamma G \Sigma_{\text{gas}} + \frac{4P_{\text{ext}}}{\Sigma_{\text{gas}}} \right), \quad (16)$$

where Γ is a geometry factor (0.6 for a sphere of constant density and 0.73 for an isothermal sphere of critical mass), σ_v^2/R is the scaling coefficient, and $\Sigma_{\text{gas}} = M/(\pi R^2)$ is the gas surface density. Note that Equation (16) is analogous to Equation (10) in the absence of the tidal force. For a given external pressure and kinetic energy, the critical mass (maximum mass) of a cloud in equilibrium is obtained by

$$\begin{aligned} \frac{\sigma_v^2}{R_c} &= \frac{1}{3} \left(\pi \Gamma G \Sigma_c + \frac{4P_{\text{ext}}}{\Sigma_c} \right) \\ &= (6.0 \text{ or } 6.4) \times 10^{-12} \left(\frac{P_{\text{ext}}}{k} \right) \text{ cm s}^{-2} \end{aligned} \quad (17)$$

where R_c and Σ_c are the critical radius and critical surface gas density, respectively. The factor 6.0 and 6.4 in Equation (17) are for centrally concentrated internal density and uniform density, respectively. The cloud mass lower than the critical mass will be gravitationally stable. We refer to Equations (2) to (5) of Field et al. (2011) for the derivation of Equation (17). In this model, the effect of tidal force is not considered. We still can make a comparison with our data as we find that the tidal force is less important in the virial equilibrium at the distance ≥ 1.5 pc (see Figure 9).

Figure 14 plots the clumps (at $r \geq 1.5$ pc) in the $\sigma_v^2/R - \Sigma_{\text{gas}}$ plane. The dot-dashed lines draw Equation (16) in the range of $P_{\text{ext}}/k_B = 10^{5-10} \text{ cm}^{-3} \text{ K}$. The solid line corresponds to $P_{\text{ext}} = 0$. In Figure 14(a), (b), the non-thermal pressure of the clumps is $10 - 10^4$ times higher than the thermal pressure. If the clumps exist in a range of different pressure environments, the clumps leftward to the critical lines could be stable if the required P_{ext} exists to confine them. Some clumps located in the region between the critical line and the $P_{\text{ext}} = 0$ line are in unstable configurations such that small perturbations would drive them to gravitational collapse. Clumps located to the right of the $P_{\text{ext}} = 0$ line are not in virial equilibrium, and would collapse if there are no other supporting forces such as magnetic forces, which are not considered in the present work. Figure 14 shows that a majority of the clumps we identified are in PVE if the external pressure is in the range of $P_{\text{ext}}/k_B = 10^{6-9} \text{ cm}^{-3} \text{ K}$. The molecular clouds in the central molecular zone (CMZ) are also proposed to be in pressure equilibrium (Miyazaki & Tsuboi 2000; Oka et al. 2001). In the GC, the external pressure of ambient X-ray amounting to $P_{\text{ext}}/k_B = (1-2) \times 10^6 \text{ cm}^{-3} \text{ K}$

(Ponti et al. 2019) is found and would be able to confine the clouds with densities of 10^{3-4} cm^{-3} , even if they have densities lower than $n_{\text{crit}0}$. Since these low density clumps are the majority population of the observed morphology, confinement via external pressure ensures a relatively steady morphology.

The external pressure required for equilibrium in the CND is 2-4 orders of magnitude higher than the typical molecular clouds in galactic disks ($P_{\text{ext}} = 10^{4-5} \text{ cm}^{-3} \text{ K}$, Bertoldi & McKee 1992; Belloche et al. 2011). If the CND is pressure-bounded, a much higher external pressure is required. External magnetic fields with a strength of 1 mG can provide an external pressure of $\sim 10^8 \text{ cm}^{-3} \text{ K}$. In addition, the hot gas from the mini-spiral also provides external pressure of $\sim 10^8 \text{ cm}^{-3} \text{ K}$ inside the CND. However, it is unclear whether these two sources provide isotropic and homogeneous confinement since (1) the magnetic field strength is subject to scale of structures and we are still unaware whether the magnetic field plays an important role on core-scale in the CND, and (2) the mini-spiral only provides confinement of the molecular clouds with narrow velocity and space. High resolution magnetic field observations made by ALMA are important to further study the CND-clouds.

5. SUMMARY

We have presented ALMA and TP array observations of 5 CS rotational lines ($J_u = 7, 5, 4, 3, 2$) in the central 10 pc of the GC. With a spatial resolution of $1.3'' = 0.05 \text{ pc}$, we are able to probe the gravitational stability of molecular clumps within the filamentary structures. Using the *astrodendro*, we identify 2379 clumps. Among these clumps, 1071 clumps are able to derive the n_{H_2} and T_k using Radex.

- The compact clouds are a mixture of warm ($T_k \geq 50 - 500 \text{ K}$, $n_{\text{H}_2} = 10^{3-5} \text{ cm}^{-3}$) and cold gas ($T_k \leq 50 \text{ K}$, $n_{\text{H}_2} = 10^{6-8} \text{ cm}^{-3}$).
- 78% of the compact clumps (fraction of number) in this region have $T_k \geq 50 \text{ K}$ and $n_{\text{H}_2} \leq 10^5 \text{ cm}^{-3}$.
- The total gas mass of these 1071 clumps is $2.5_{-0.4}^{+1.0} \times 10^4 M_\odot$. 1009 clumps are tidally unstable and account for $16_{-7.5}^{+28} \%$ of the total gas mass. However, we find that although the tidal force may affect the cloud morphology of the lower density gas, a part of them can be confined by external pressure from X-ray emission.
- $28_{-12}^{+24} \%$ of the total gas mass is tidally stable, but will not collapse to form stars.

Based on the unmagnetized virial theorem including tidal force, we study the behavior of the molecular gas and the possibility of star formation in the CND.

- At a distance ≥ 1.5 pc from Sgr A*, turbulence dominates the internal energy and sets the nearly constant threshold densities of $3 \times 10^7 \text{ cm}^{-3}$, which inhibits the clumps from collapsing to form stars.
- 56^{+22}_{-28} % of the total gas mass is able to form stars. However, there is no clear evidence of on-going star formation, these seemingly-unstable clumps should be marginally stabilized by other forces such as magnetic fields.
- Within the central 1.5 pc, tidal force again dominates the gravitational stability and the threshold densities quickly rise to $\geq 10^8 \text{ cm}^{-3}$, which strongly inhibit star formations.

ACKNOWLEDGMENTS

We are grateful to the referee for a thorough and insightful report which helped to improve the paper. P.-Y. H. was supported by the Ministry of Science and Technology (MoST) of Taiwan through the grants MOST 108-2112-M-001-012 and MOST 109-2112-M-001-022. The work of W.-T. K. was supported by the grants of National Research Foundation of Korea (2019R1A2C1004857 and 2020R1A4A2002885). Jean L. Turner was supported by the NSF grant AST 2006433. This paper makes use of the following ALMA data: ADS/JAO.ALMA#2017.1.00040.S. ALMA is a partnership of ESO (representing its member states), NSF (USA) and NINS (Japan), together with NRC (Canada), MOST and ASIAA (Taiwan), and KASI (Republic of Korea), in cooperation with the Republic of Chile. The Joint ALMA Observatory is operated by ESO, AUI/NRAO and NAOJ.

Facilities: ALMA

Software: `astrodendro` (Rosolowsky et al. 2008), `Radex` (van der Tak et al. 2007),

APPENDIX

Here we display the channel map of CS(7-6) line (Figure 15), the density-distance relation for clumps with uncertainties less than 1 order of magnitude (Figure 16), and various physical quantities of clumps in the deprojected map (Figure 17).

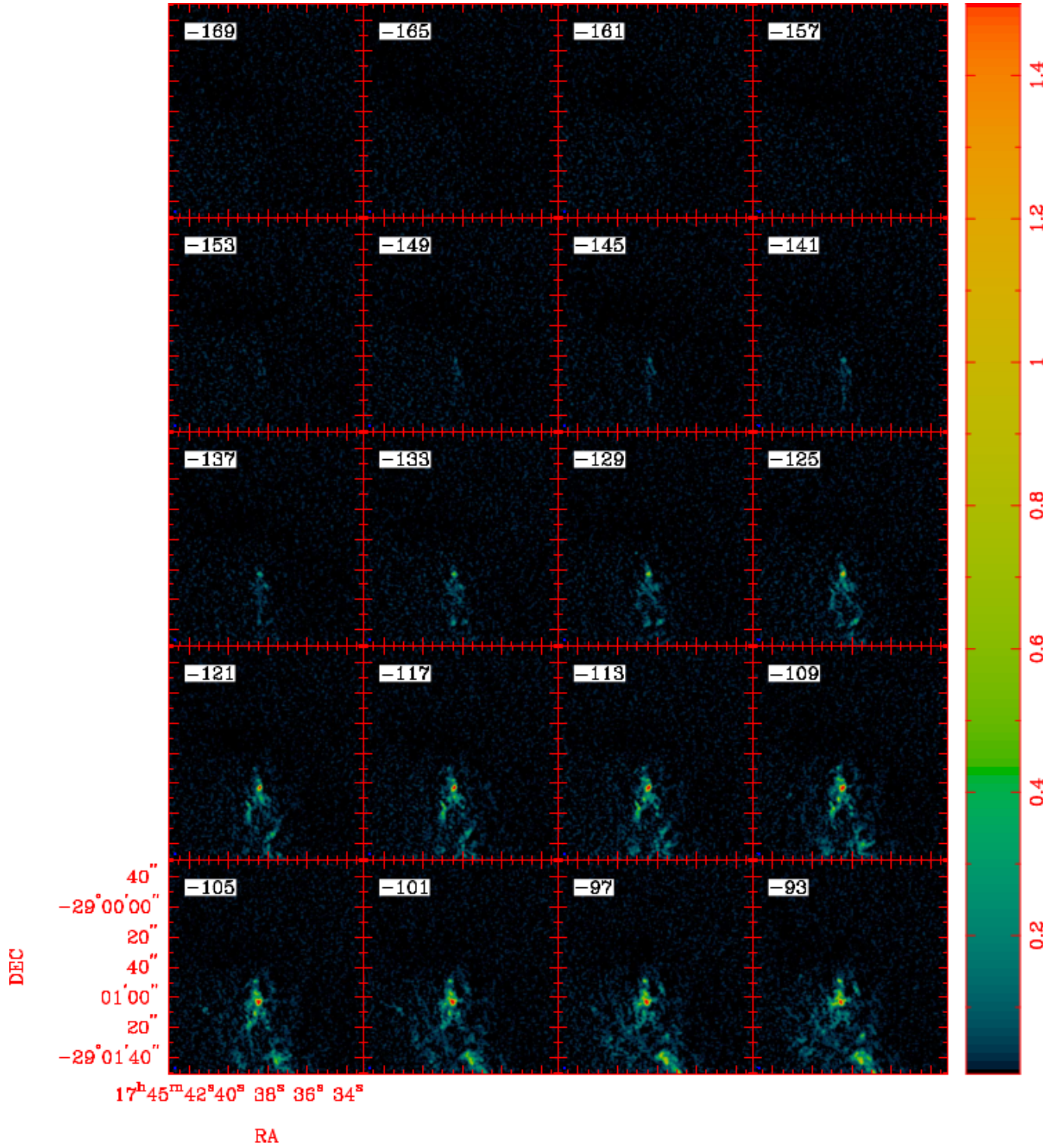
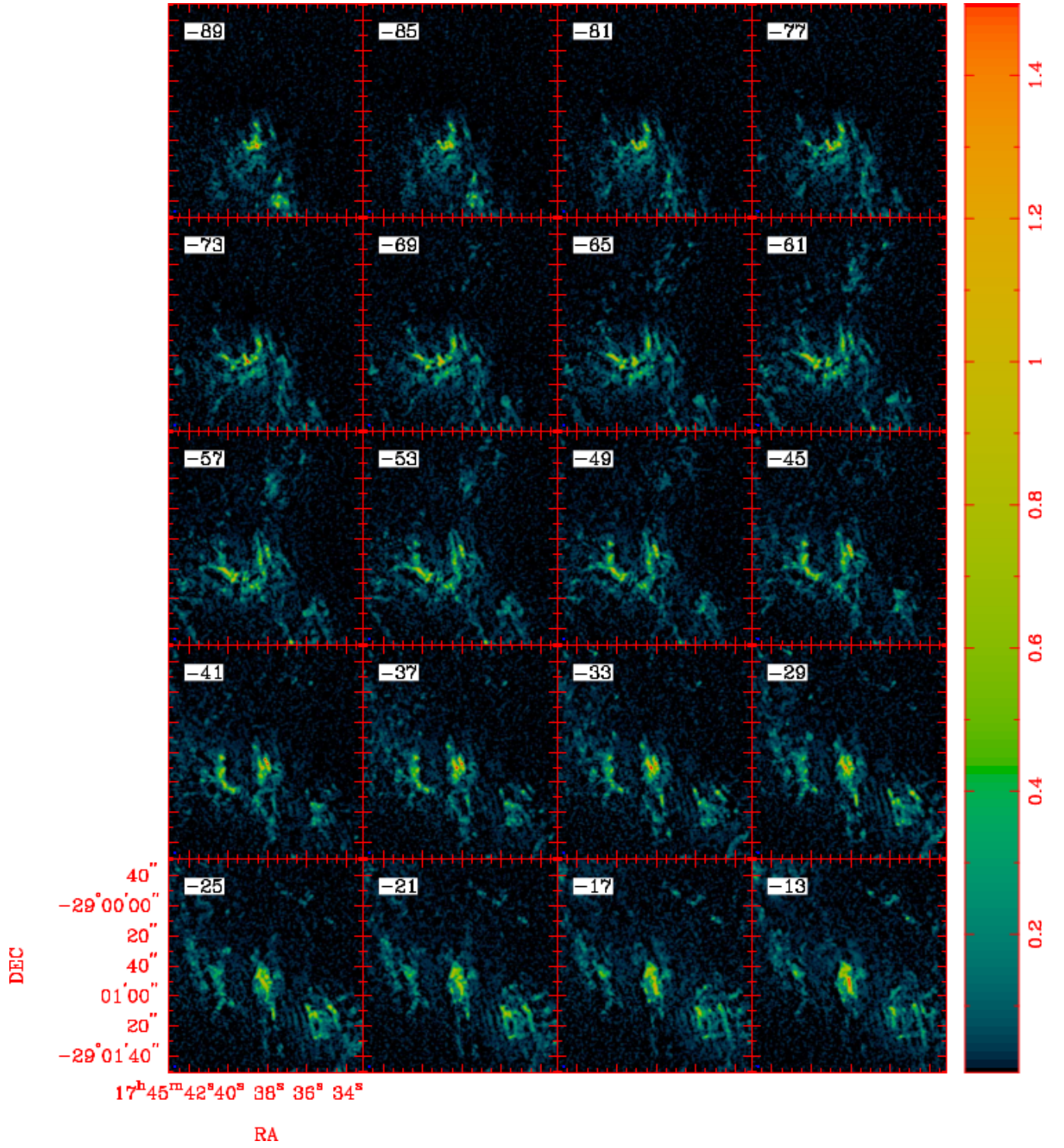


Figure 15. Channel map of the CS(7-6) line. The velocity width is binned to 4 km s^{-1} to reduce the numbers of panels. The LSR velocity is labeled on the top left corner in unit of km s^{-1} . The intensity unit of Jy beam^{-1} (beam= $1.3''$).



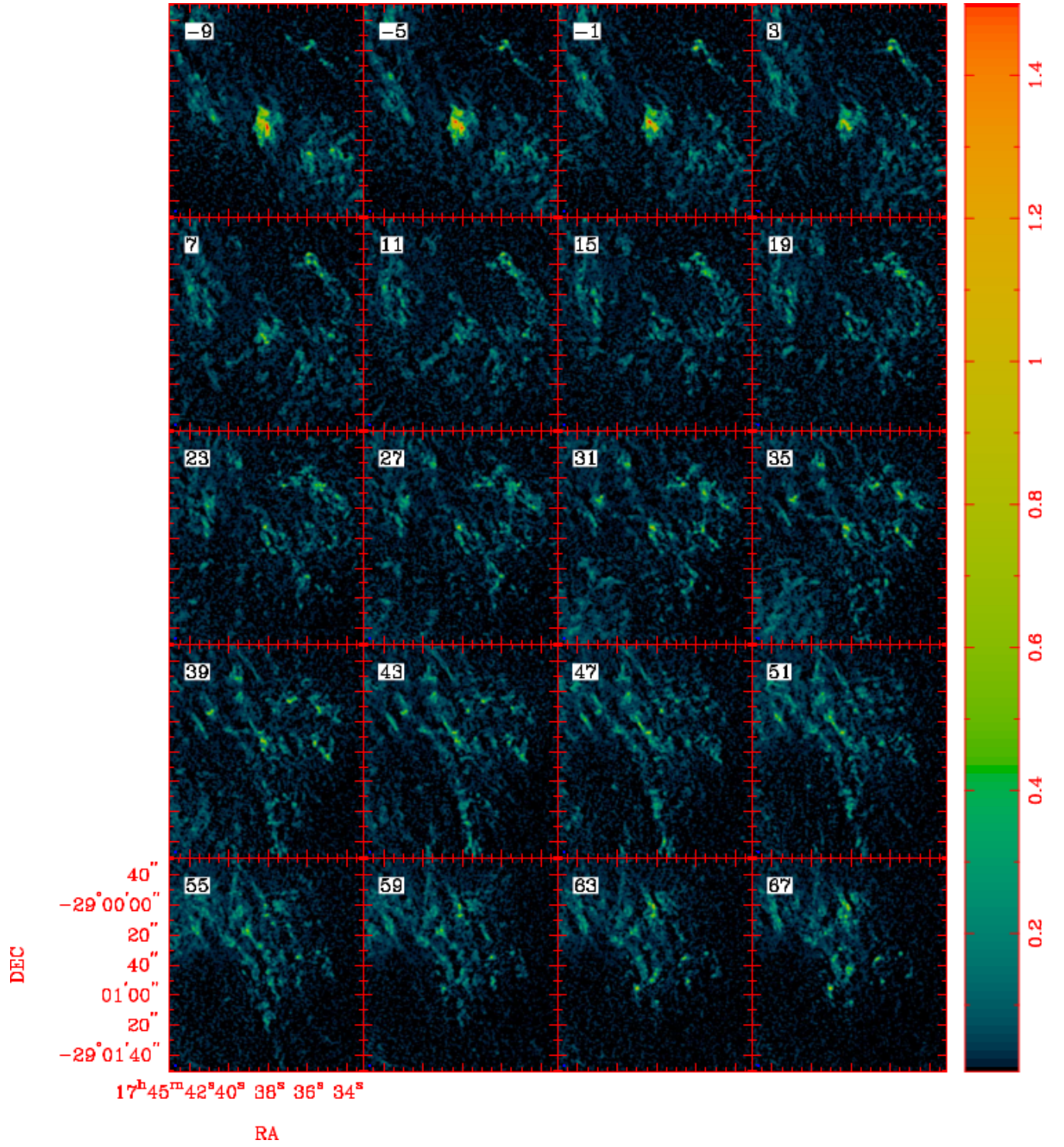


Figure 15. Continued.

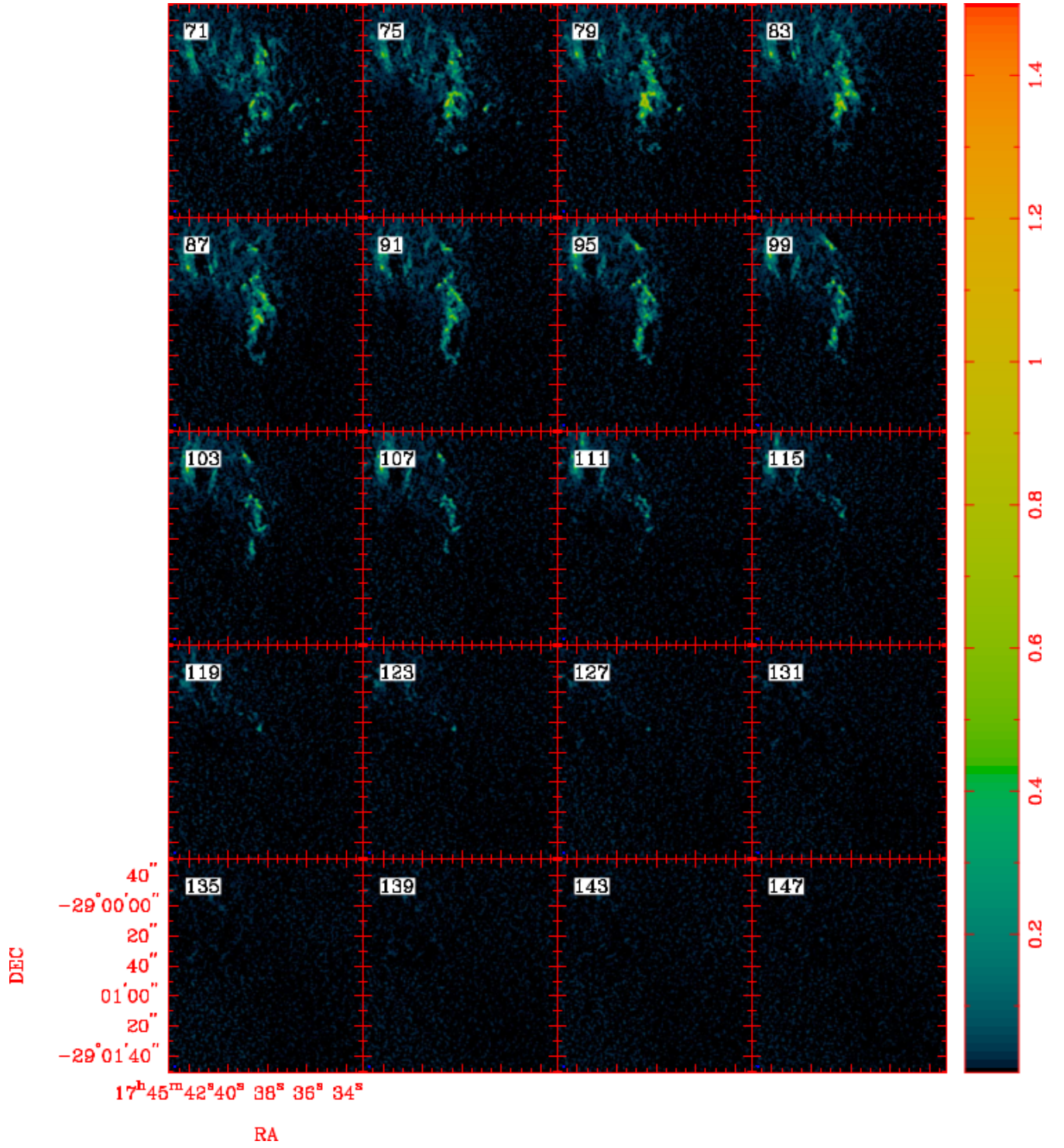


Figure 15. Continued.

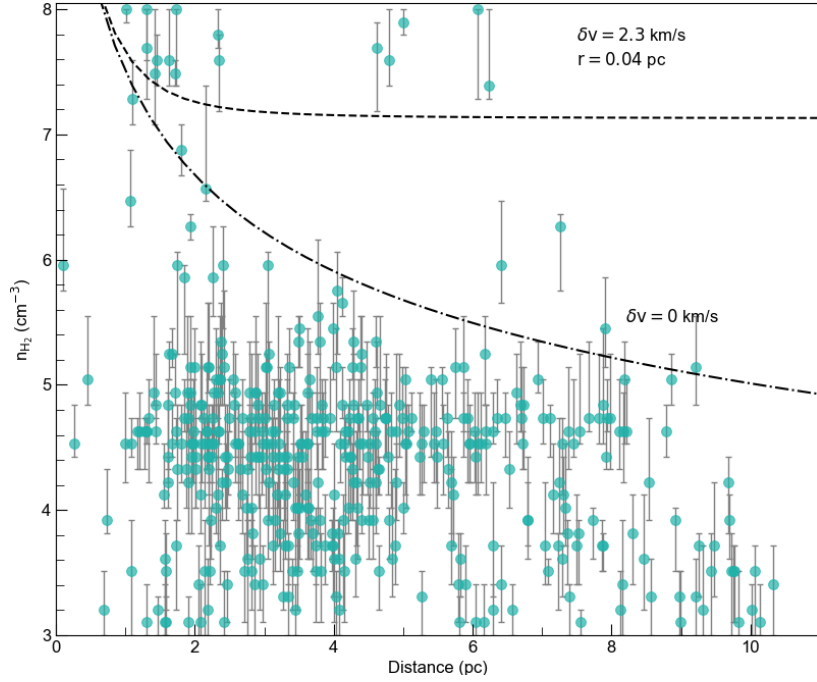


Figure 16. Same as Figure 9, but the densities with uncertainties less than 1 order of magnitude are shown. Clumps with densities having upper limit ($\leq 10^8 \text{ cm}^{-3}$) are also presented.)

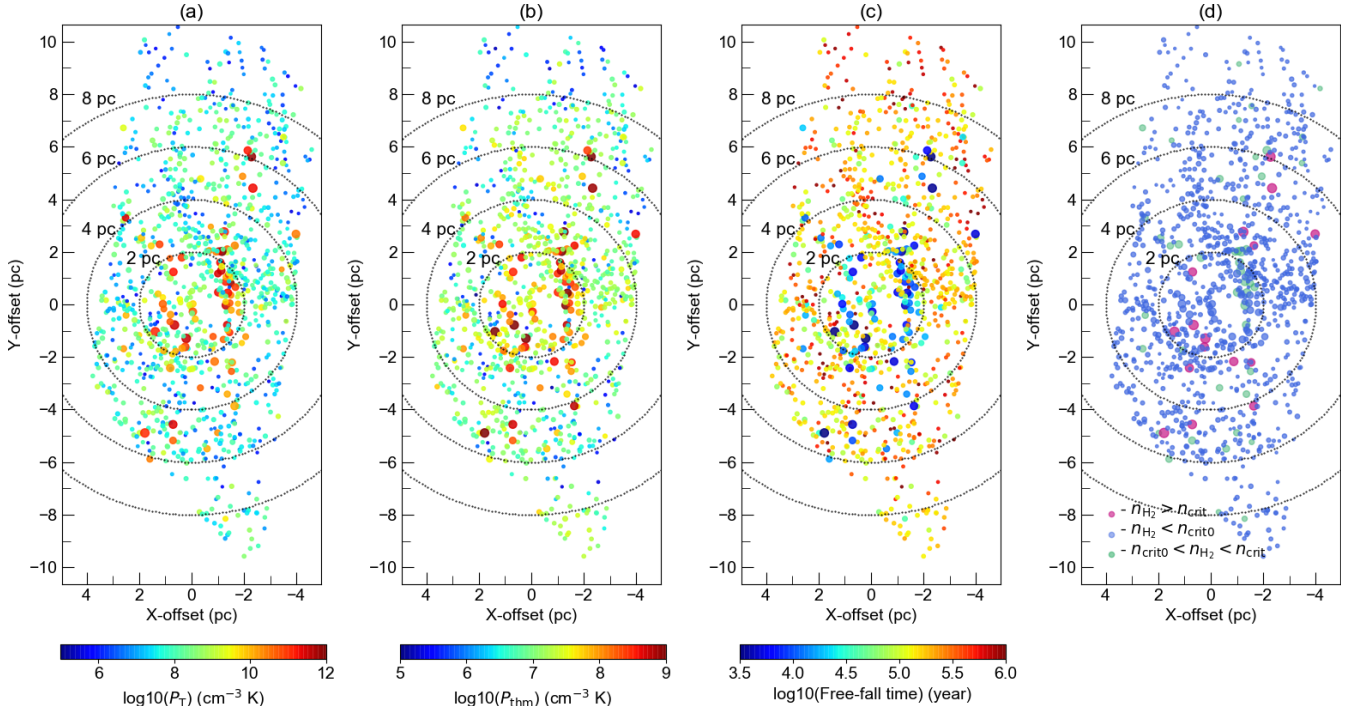


Figure 17. Clumps shown in the deprojected map. (a) colors represent the turbulence pressure of clumps. (b) colors represent the thermal pressure of clumps (c) colors represent the free-fall time τ_{ff} of clumps. The free-fall time (τ_{ff}) is calculated as $\tau_{\text{ff}} = \sqrt{\frac{3\pi}{32G\rho_{\text{gas}}}}$. (d) blue circles are clumps below n_{crit0} (dispersed by tidal force). Green circles are clumps within n_{crit0} and n_{crit} (stable clumps). Red circles are clumps above n_{crit} (able to collapse to form stars). The circle sizes are proportional to n_{H_2} .

Table 1. *CS Lines*

Transition	Rest Frequency (GHz)	E_u (K)	Critical Density (cm^{-3})
2–1	97.980	7.1	3.9×10^5
3–2	146.969	14.1	1.2×10^6
4–3	195.954	23.5	2.8×10^6
5–4	244.935	35.5	5.5×10^6
7–6	344.882	65.8	1.5×10^7

The collisional critical density is calculated with the Einstein coefficients and collisional rates ([Lique et al. 2006](#)) from LAMDA data base at kinetic temperature of 60 K.

Table 2. *12m-Mosaic Observation*

Line	Frequency [GHz]	$\Delta f/\Delta v$ [kHz/km s ⁻¹]	Date	EB	Antennas	Pointing	Baseline [m]/[k λ]	Integration [min]
(1)	(2)	(3)	(4)	(5)	(6)	(7)	(8)	(9)
CS(2-1)	97.980	282.3/1.0	2017-12-24	X317f	43	68	15-2517/4.9-822	14
			2018-06-05	X16ec	50	68	15-360/4.9-118	7
CS(3-2)	146.969	564.5/1.3	2018-03-15	X1daef	43	138	15-784/7.3-384	28
CS(4-3)	195.954	564.5/0.9	2018-08-19	X16d2	43	150	15-457/9.8-298	34
			2019-03-28	X2858	44	101	15-500/9.8-326	20
			2018-12-23	X12445	45	101	15-500/9.8-326	20
			2018-08-17	X81da	43	101	15-500/9.8-326	20
CS(5-4)	244.936	1129/1.4	2018-03-27	X4b71	43	150	15-784/12-640	30
			2018-03-27	X57af	44	150	15-784/12-640	30
CS(7-6)	342.883	1129/1.0	2018-05-01	X2f73	43	150	15-500/17-571	45
			2018-04-19	X86f1	44	150	15-500/17-571	45
			2018-04-07	X922b	43	150	15-484/17-553	44
			2018-04-07	X78b3	43	150	15-484/17-553	45
			2018-04-18	X9e23	45	150	15-500/17-571	45

(1)target line and the ALMA band. (2) line rest frequency. (3) default spectral resolution in frequency and velocity. (4) observing date.(5) name of ALMA execution blocks (EB). (6) number of antennas used in the observation. (7) number of pointings for mosaic observation. (8) baselines of configuration used for the observation. The min/max baseline lengths are in meter and $k\lambda$. (9) on-source integration time.

Table 3. *7m-Mosaic Observation*

Line	Frequency [GHz]	Date	EB	Antennas	Pointing	Baseline [m]/[k λ]	Integration [min]
(1)	(2)	(3)	(4)	(5)	(6)	(7)	(8)
CS(2-1)	97.980	2017-11-06	X21e	9	27	9–49/2.9–16	41
		2017-10-10	X3fe1	9	27	9–49/2.9–16	41
CS(3-2)	146.969	2017-10-19	X467	10	45	9–49/4.4–24	45
		2017-10-17	X3a8	10	45	9–49/4.4–24	45
		2017-10-14	X287	11	45	9–49/4.4–24	45
CS(4-3)	195.954	2018-05-02	Xbf98	10	73	9–48/5.9–31	49
		2019-05-02	Xb438	10	73	9–48/5.9–31	49
		2018-04-29	X2a34	10	73	9–48/5.9–31	49
		2018-04-29	X1fd9	10	52	9–49/5.9–32	44
		2018-04-29	X198f	10	52	9–49/5.9–32	44
CS(5-4)	244.936	2017-10-04	X2aa	11	74	9–49/7.3–37	50
		2017-10-03	X8544	9	74	9–45/7.3–40	50
		2017-10-03	X80dd	9	74	9–45/7.3–40	50
		2017-10-23	X179	10	79	9–49/7.3–37	40
		2017-10-20	X6aa	10	79	9–49/7.3–37	40
		2017-10-19	X4c42	10	79	9–49/7.3–37	40
		2017-10-19	X4981	10	79	9–49/7.3–37	40
CS(7-6)	342.883	2017-12-12	X4d74	10	70	9–49/10.3–56	47
		2017-10-08	X47d7	9	70	9–49/10.3–56	47
		2017-10-06	X39e	11	70	9–49/10.3–56	47
		2017-10-03	X704	11	70	9–49/10.3–56	47
		2018-03-11	X355d	10	67	9–49/10.3–56	45
		2018-03-10	X522a	10	67	9–49/10.3–56	45
		2018-01-21	X69f0	11	67	9–49/10.3–56	45
		2018-01-20	X597e	11	67	9–49/10.3–56	45
		2018-04-19	X57e6	10	75	9–49/10.3–56	38
		2018-04-11	X12b91	10	75	9–49/10.3–56	38
		2018-04-07	X50f2	11	75	9–49/10.3–56	38
		2018-04-02	Xb7a8	11	75	9–45/10.3–56	38
		2018-04-02	Xb219	11	75	9–45/10.3–51	38
		2018-04-19	X6b30	10	75	9–49/10.3–56	38
		2018-04-12	X505c	10	75	9–49/10.3–56	38
		2018-03-24	X5a09	11	75	9–49/10.3–56	38
		2018-03-10	X603e	11	75	9–45/10.3–51	38
		2018-01-21	X5ec2	11	75	9–45/10.3–51	38

(1) target line and the ALMA band. (2) rest frequency of the line. (3) observing date.(4) name of ALMA execution blocks. (5) number of antennas used in the observation. (6) number of pointing for mosaic observation. (7) baselines of configuration used for the observation. The min/max baseline lengths are in meter and kilo- λ . (8) on-source integration time.

Table 4. *Total Power Observation*

Line	Frequency (GHz)	Date	EB	Antennas	Integrtrion (min)
(1)	(2)	(3)	(4)	(5)	(6)
CS(2-1)	97.980	2018-01-17	Xd65f	3	54
		2018-01-04	X82fd	3	54
		2018-01-04	X7a47	3	54
CS(3-2)	146.969	2018-01-09	X7322	3	59
		2018-01-09	X696e	3	59
		2018-01-07	X7b59	3	59
		2018-01-04	X8a3d	3	59
		2017-12-27	Xfc40	2	59
CS(4-3)	195.954	2018-06-18	X2191	3	53
		2018-06-18	X1c3a	3	53
		2018-05-25	Xd7b6	3	53
		2018-05-02	Xc804	4	53
		2018-05-02	Xbd2f	4	53
		2018-05-02	Xb37f	4	53
		2018-12-11	X71bb	3	53
		2018-05-25	Xce26	3	53
		2018-04-29	X39bc	2	53
		2018-04-29	X2b63	2	53
		2018-04-07	X97d5	3	38
		2018-03-27	X6320	3	42
CS(5-4)	244.936	2018-03-16	X6d6e	3	52
		2018-03-16	X63e1	3	52
		2018-03-13	X53fc	3	52
		2018-03-09	X2b3c	3	52
		2018-03-09	X229d	3	52
		2018-01-23	X6d48	3	52
		2018-04-04	X3599	4	51
		2018-04-01	X1f93	3	51
		2018-03-31	X45dd	3	18
		2018-03-31	X35a5	3	52
		2018-03-30	X2821	3	48
		2018-03-23	X2ff4	3	51
CS(7-6)	342.883	2018-04-05	Xb461	4	53
		2018-04-05	Xb0ae	4	13
		2018-04-04	X4ec9	2	53
		2018-04-04	X3ff0	4	53
		2018-04-01	X3355	3	53
		2018-03-26	X65bb	3	53
		2018-03-24	X7525	3	53
		2018-03-24	X5b20	3	53
		2018-05-15	X3936	3	56
		2018-05-13	X25e1	3	56
		2018-05-13	X33d	3	56
		2018-05-09	X58c4	3	53
		2018-05-07	Xedef	3	53

2018-05-07	Xc4d7	3	53
2018-05-03	X3d00	4	47
2018-05-03	X2791	4	56
2018-04-18	Xa915	3	56
2018-05-03	X1cb5	4	50
2018-04-27	X91cd	4	50
2018-04-20	X10bda	4	50
2018-04-19	X8e40	4	50
2018-04-19	X595e	4	50
2018-04-06	X8011	4	47
2018-04-06	X5e0e	4	50
2018-04-03	X3bf7	3	50
2018-04-03	X29a7	3	50
2018-08-20	Xa5b3	3	55
2018-08-19	X1058	3	55
2018-08-17	X73be	3	55
2018-06-21	X256e	4	55
2018-05-17	X35ad	3	55
2018-05-16	Xd61f	2	55
2018-05-14	X2864	3	55
2018-05-14	X1b7c	3	55

(1)target line and the ALMA band. (2) rest frequency of the line. (3) observing date.(4) name of ALMA execution blocks. (5) number of antennas used in the observation. (6) on-source integration time.

Table 5. *Gas mass of the 1071 clumps*

Type of clumps	Gas mass ($10^4 M_\odot$)	$f_{\text{gas}}^{(4)}$ (%)	Number of clumps
(1) $n_{\text{H}_2} < n_{\text{crit}0}$	$0.4^{+0.7}_{-0.1}$	$16^{+28}_{-7.5}$	1009
(2) $n_{\text{crit}0} < n_{\text{H}_2} < n_{\text{crit}}$	$0.7^{+0.6}_{-0.1}$	28^{+24}_{-12}	46
(3) $n_{\text{H}_2} > n_{\text{crit}}$	$1.4^{+0.5}_{-0.4}$	56^{+22}_{-28}	16

(1) clumps with n_{H_2} lower than tidal threshold, (2) clumps gravitationally stable, (3) clumps are able to collapse to form stars, (4) f_{gas} is the fraction of total gas mass. The total gas mass is $2.5^{+1.0}_{-0.4} \times 10^4 M_\odot$.

Table 6. *Clumps above n_{crit}*

ID	RA. (J2000)	Dec. (J2000)	R_s	V_{cen}	σ_{vden}	T_k	n_{H_2}	M_{gas}
			(pc)	(km s $^{-1}$)	(km s $^{-1}$)	(K)	(cm $^{-3}$)	(M_\odot)
(1)	(2)	(3)	(4)	(5)	(6)	(7)	(8)	(9)
446	17:45:40.40	-29:01:13.04	0.036 ± 0.009	-105.1	1.5 ± 0.6	20^{+500}_{-10}	$7.18^{+0.82}_{-2.45}$	206^{+1140}_{-205}
933	17:45:37.40	-29:00:50.34	0.022 ± 0.006	-60.8	1.6 ± 0.8	$10^{+10}_{-7.27}$	$8.00^{+0.00}_{-1.22}$	291^{+0}_{-273}
974	17:45:41.40	-29:01:20.52	0.023 ± 0.009	-59.4	0.9 ± 0.4	20^{+230}_{-10}	$7.49^{+0.51}_{-2.14}$	109^{+244}_{-108}
1076	17:45:40.83	-29:00:56.52	0.026 ± 0.007	-49.0	1.3 ± 0.5	$10^{+10}_{-7.27}$	$7.59^{+0.20}_{-0.41}$	196^{+118}_{-120}
1272	17:45:35.58	-29:01:58.18	0.025 ± 0.007	-34.7	1.2 ± 0.6	$10^{+10}_{-7.27}$	$7.59^{+0.41}_{-0.20}$	165^{+258}_{-62}
1281	17:45:34.85	-29:01:07.11	0.051 ± 0.004	-29.8	3.8 ± 0.5	$10^{+10}_{-7.27}$	$8.00^{+0.00}_{-0.71}$	3693^{+0}_{-2980}
1422	17:45:35.58	-29:01:12.27	0.038 ± 0.005	-26.0	2.3 ± 0.4	$10^{+10}_{-7.27}$	$7.90^{+0.10}_{-0.10}$	1268^{+336}_{-265}
1709	17:45:44.41	-28:59:59.25	0.036 ± 0.007	-16.0	1.5 ± 0.4	$10^{+110}_{-7.27}$	$8.00^{+0.00}_{-2.76}$	1267^{+0}_{-1265}
2251	17:45:41.01	-29:00:27.12	0.030 ± 0.004	7.2	2.7 ± 0.5	$10^{+10}_{-7.27}$	$8.00^{+0.00}_{-0.71}$	742^{+0}_{-599}
2565	17:45:41.65	-28:59:57.19	0.026 ± 0.007	17.3	1.6 ± 0.5	$10^{+10}_{-7.27}$	$8.00^{+0.00}_{-0.61}$	502^{+0}_{-380}
2851	17:45:41.24	-29:00:27.12	0.034 ± 0.006	27.3	1.9 ± 0.5	$10^{+10}_{-7.27}$	$7.59^{+0.41}_{-0.20}$	437^{+681}_{-164}
3044	17:45:40.99	-29:00:14.48	0.030 ± 0.005	35.5	2.6 ± 0.6	$10^{+10}_{-7.27}$	$8.00^{+0.00}_{-0.10}$	798^{+0}_{-167}
3440	17:45:43.46	-29:00:24.79	0.049 ± 0.007	50.2	3.2 ± 0.4	$10^{+10}_{-7.27}$	$7.69^{+0.20}_{-0.51}$	1601^{+960}_{-1106}
3446	17:45:39.71	-29:00:07.25	0.058 ± 0.005	51.5	3.3 ± 0.4	$10^{+10}_{-7.27}$	$7.49^{+0.51}_{-0.41}$	1704^{+3809}_{-1038}
3581	17:45:37.46	-29:01:01.94	0.044 ± 0.010	51.7	1.6 ± 0.3	20^{+500}_{-10}	$7.29^{+0.61}_{-2.14}$	449^{+1390}_{-446}
3659	17:45:42.15	-29:00:15.51	0.044 ± 0.009	53.3	1.0 ± 0.1	$10^{+500}_{-7.27}$	$7.49^{+0.51}_{-3.06}$	719^{+1607}_{-718}

(1) the ID of clumps, (2), (3) the positions of clumps, (4) the effective radius (R_s) of clumps, (5) the central velocities of clumps, (6) the velocity dispersion derived in astrodendro, (7) kinetic temperature, (8) volume density of H_2 , (9) gas mass. Note that 5 out of them have large uncertainties of T_k and n_{H_2} (ID=446, 974, 1079, 3581, 3659).

REFERENCES

- Athanassoula, E. 1992, MNRAS, 259, 345,
doi: [10.1093/mnras/259.2.345](https://doi.org/10.1093/mnras/259.2.345)
- Belloche, A., Schuller, F., Parise, B., et al. 2011, A&A, 527, A145, doi: [10.1051/0004-6361/201015733](https://doi.org/10.1051/0004-6361/201015733)
- Bertoldi, F., & McKee, C. F. 1992, ApJ, 395, 140,
doi: [10.1086/171638](https://doi.org/10.1086/171638)
- Bradford, C. M., Stacey, G. J., Nikola, T., et al. 2005, ApJ, 623, 866, doi: [10.1086/428659](https://doi.org/10.1086/428659)
- Christopher, M. H., Scoville, N. Z., Stolovy, S. R., & Yun, M. S. 2005, ApJ, 622, 346, doi: [10.1086/427911](https://doi.org/10.1086/427911)
- Collin, S., & Zahn, J.-P. 1999, A&A, 344, 433
- Combes, F., García-Burillo, S., Audibert, A., et al. 2019, A&A, 623, A79, doi: [10.1051/0004-6361/201834560](https://doi.org/10.1051/0004-6361/201834560)
- Field, G. B., Blackman, E. G., & Keto, E. R. 2011, MNRAS, 416, 710, doi: [10.1111/j.1365-2966.2011.19091.x](https://doi.org/10.1111/j.1365-2966.2011.19091.x)
- Figer, D. F., Kim, S. S., Morris, M., et al. 1999, ApJ, 525, 750, doi: [10.1086/307937](https://doi.org/10.1086/307937)

- Genzel, R., Crawford, M. K., Townes, C. H., & Watson, D. M. 1985, *ApJ*, 297, 766, doi: [10.1086/163574](https://doi.org/10.1086/163574)
- Ghez, A. M., Salim, S., Hornstein, S. D., et al. 2005, *ApJ*, 620, 744, doi: [10.1086/427175](https://doi.org/10.1086/427175)
- Goicoechea, J. R., Pety, J., Chapillon, E., et al. 2018, *A&A*, 618, A35, doi: [10.1051/0004-6361/201833558](https://doi.org/10.1051/0004-6361/201833558)
- Goldreich, P., & Kwan, J. 1974, *ApJ*, 189, 441, doi: [10.1086/152821](https://doi.org/10.1086/152821)
- Goldsmith, P. F., & Kauffmann, J. 2017, *ApJ*, 841, 25, doi: [10.3847/1538-4357/aa6f12](https://doi.org/10.3847/1538-4357/aa6f12)
- Güsten, R., & Downes, D. 1980, *A&A*, 87, 6
- Harada, N., Riquelme, D., Viti, S., et al. 2015, *ArXiv e-prints*. <https://arxiv.org/abs/1510.02904>
- Herrnstein, R. M., & Ho, P. T. P. 2005, *ApJ*, 620, 287, doi: [10.1086/426047](https://doi.org/10.1086/426047)
- Hopkins, P. F., & Quataert, E. 2010, *MNRAS*, 407, 1529, doi: [10.1111/j.1365-2966.2010.17064.x](https://doi.org/10.1111/j.1365-2966.2010.17064.x)
- Hsieh, P.-Y., Koch, P. M., Ho, P. T. P., et al. 2017, *ApJ*, 847, 3, doi: [10.3847/1538-4357/aa8329](https://doi.org/10.3847/1538-4357/aa8329)
- Hsieh, P.-Y., Koch, P. M., Kim, W.-T., et al. 2018, *ApJ*, 862, 150, doi: [10.3847/1538-4357/aacb27](https://doi.org/10.3847/1538-4357/aacb27)
- . 2019, *ApJL*, 885, L20, doi: [10.3847/2041-8213/ab4e1e](https://doi.org/10.3847/2041-8213/ab4e1e)
- Hsieh, P.-Y., Matsushita, S., Liu, G., et al. 2011, *ApJ*, 736, 129, doi: [10.1088/0004-637X/736/2/129](https://doi.org/10.1088/0004-637X/736/2/129)
- Imanishi, M., Nakanishi, K., Izumi, T., & Wada, K. 2018, *ApJL*, 853, L25, doi: [10.3847/2041-8213/aaa8df](https://doi.org/10.3847/2041-8213/aaa8df)
- Izumi, T., Wada, K., Fukushima, R., Hamamura, S., & Kohno, K. 2018, *ApJ*, 867, 48, doi: [10.3847/1538-4357/aae20b](https://doi.org/10.3847/1538-4357/aae20b)
- Jackson, J. M., Geis, N., Genzel, R., et al. 1993, *ApJ*, 402, 173, doi: [10.1086/172120](https://doi.org/10.1086/172120)
- Kim, W.-T., Seo, W.-Y., & Kim, Y. 2012, *ApJ*, 758, 14, doi: [10.1088/0004-637X/758/1/14](https://doi.org/10.1088/0004-637X/758/1/14)
- Krumholz, M. R. 2011, in *American Institute of Physics Conference Series*, Vol. 1386, XV Special Courses at the National Observatory of Rio de Janeiro, ed. E. Telles, R. Dupke, & D. Lazzaro, 9–57, doi: [10.1063/1.3636038](https://doi.org/10.1063/1.3636038)
- Levin, Y., & Beloborodov, A. M. 2003, *ApJL*, 590, L33, doi: [10.1086/376675](https://doi.org/10.1086/376675)
- Lin, L.-H., Wang, H.-H., Hsieh, P.-Y., et al. 2013, *ApJ*, 771, 8, doi: [10.1088/0004-637X/771/1/8](https://doi.org/10.1088/0004-637X/771/1/8)
- Lique, F., Spielfiedel, A., & Cernicharo, J. 2006, *A&A*, 451, 1125, doi: [10.1051/0004-6361:20054363](https://doi.org/10.1051/0004-6361:20054363)
- Liu, H. B., Ho, P. T. P., Wright, M. C. H., et al. 2013, *ApJ*, 770, 44, doi: [10.1088/0004-637X/770/1/44](https://doi.org/10.1088/0004-637X/770/1/44)
- Liu, H. B., Hsieh, P.-Y., Ho, P. T. P., et al. 2012, *ApJ*, 756, 195, doi: [10.1088/0004-637X/756/2/195](https://doi.org/10.1088/0004-637X/756/2/195)
- Marr, J. M., Wright, M. C. H., & Backer, D. C. 1993, *ApJ*, 411, 667, doi: [10.1086/172869](https://doi.org/10.1086/172869)
- Martín, S., Martín-Pintado, J., Montero-Castaño, M., Ho, P. T. P., & Blundell, R. 2012, *A&A*, 539, A29, doi: [10.1051/0004-6361/201117268](https://doi.org/10.1051/0004-6361/201117268)
- Mills, E. A. C., Güsten, R., Requena-Torres, M. A., & Morris, M. R. 2013, *ApJ*, 779, 47, doi: [10.1088/0004-637X/779/1/47](https://doi.org/10.1088/0004-637X/779/1/47)
- Miyazaki, A., & Tsuboi, M. 2000, *ApJ*, 536, 357, doi: [10.1086/308899](https://doi.org/10.1086/308899)
- Montero-Castaño, M., Herrnstein, R. M., & Ho, P. T. P. 2009, *ApJ*, 695, 1477, doi: [10.1088/0004-637X/695/2/1477](https://doi.org/10.1088/0004-637X/695/2/1477)
- Oka, T., Hasegawa, T., Sato, F., et al. 2001, *ApJ*, 562, 348, doi: [10.1086/322976](https://doi.org/10.1086/322976)
- Oka, T., Nagai, M., Kamegai, K., & Tanaka, K. 2011, *ApJ*, 732, 120, doi: [10.1088/0004-637X/732/2/120](https://doi.org/10.1088/0004-637X/732/2/120)
- Paumard, T., Maillard, J. P., & Morris, M. 2004, *A&A*, 426, 81, doi: [10.1051/0004-6361:20034209](https://doi.org/10.1051/0004-6361:20034209)
- Pihlström, Y. M., Sjouwerman, L. O., & Fish, V. L. 2011, *ApJL*, 739, L21, doi: [10.1088/2041-8205/739/1/L21](https://doi.org/10.1088/2041-8205/739/1/L21)
- Ponti, G., Hofmann, F., Churazov, E., et al. 2019, *Nature*, 567, 347, doi: [10.1038/s41586-019-1009-6](https://doi.org/10.1038/s41586-019-1009-6)
- Requena-Torres, M. A., Güsten, R., Weiß, A., et al. 2012, *A&A*, 542, L21, doi: [10.1051/0004-6361/201219068](https://doi.org/10.1051/0004-6361/201219068)
- Roberts, D. A., & Goss, W. M. 1993, *ApJS*, 86, 133, doi: [10.1086/191773](https://doi.org/10.1086/191773)
- Rosolowsky, E., & Leroy, A. 2006, *PASP*, 118, 590, doi: [10.1086/502982](https://doi.org/10.1086/502982)
- Rosolowsky, E. W., Pineda, J. E., Kauffmann, J., & Goodman, A. A. 2008, *ApJ*, 679, 1338, doi: [10.1086/587685](https://doi.org/10.1086/587685)
- Sakamoto, K., Okumura, S. K., Ishizuki, S., & Scoville, N. Z. 1999, *ApJ*, 525, 691, doi: [10.1086/307910](https://doi.org/10.1086/307910)
- Schöier, F. L., van der Tak, F. F. S., van Dishoeck, E. F., & Black, J. H. 2005, *A&A*, 432, 369, doi: [10.1051/0004-6361:20041729](https://doi.org/10.1051/0004-6361:20041729)
- Shukla, H., Yun, M. S., & Scoville, N. Z. 2004, *ApJ*, 616, 231, doi: [10.1086/424868](https://doi.org/10.1086/424868)
- Sjouwerman, L. O., Pihlström, Y. M., & Fish, V. L. 2010, *ApJL*, 710, L111, doi: [10.1088/2041-8205/710/2/L111](https://doi.org/10.1088/2041-8205/710/2/L111)
- Solomon, P. M., Rivolo, A. R., Barrett, J., & Yahil, A. 1987, *ApJ*, 319, 730, doi: [10.1086/165493](https://doi.org/10.1086/165493)
- Sormani, M. C., & Barnes, A. T. 2019, *MNRAS*, 484, 1213, doi: [10.1093/mnras/stz046](https://doi.org/10.1093/mnras/stz046)
- Trani, A. A., Mapelli, M., & Ballone, A. 2018, *ApJ*, 864, 17, doi: [10.3847/1538-4357/aad414](https://doi.org/10.3847/1538-4357/aad414)
- Tress, R. G., Sormani, M. C., Glover, S. C. O., et al. 2020, *MNRAS*, 499, 4455, doi: [10.1093/mnras/staa3120](https://doi.org/10.1093/mnras/staa3120)
- Tsuboi, M., Handa, T., & Ukita, N. 1999, *ApJS*, 120, 1, doi: [10.1086/313165](https://doi.org/10.1086/313165)

- Tsuboi, M., Kitamura, Y., Uehara, K., et al. 2018, PASJ, 70, 85, doi: [10.1093/pasj/psy080](https://doi.org/10.1093/pasj/psy080)
- van der Tak, F. F. S., Black, J. H., Schöier, F. L., Jansen, D. J., & van Dishoeck, E. F. 2007, A&A, 468, 627, doi: [10.1051/0004-6361:20066820](https://doi.org/10.1051/0004-6361:20066820)
- Vollmer, B., & Duschl, W. J. 2000, New Astronomy, 4, 581, doi: [10.1016/S1384-1076\(99\)00043-3](https://doi.org/10.1016/S1384-1076(99)00043-3)
- White, G. J., Smith, H. A., Stacey, G., et al. 2003, arXiv e-prints, astro. <https://arxiv.org/abs/astro-ph/0311611>
- Wright, M. C. H., Coil, A. L., McGary, R. S., Ho, P. T. P., & Harris, A. I. 2001, ApJ, 551, 254, doi: [10.1086/320089](https://doi.org/10.1086/320089)
- Yusef-Zadeh, F., Braatz, J., Wardle, M., & Roberts, D. 2008, ApJL, 683, L147, doi: [10.1086/591731](https://doi.org/10.1086/591731)
- Yusef-Zadeh, F., Wardle, M., Sewilo, M., et al. 2015, ApJ, 808, 97, doi: [10.1088/0004-637X/808/1/97](https://doi.org/10.1088/0004-637X/808/1/97)
- Zhao, J.-H., Morris, M. R., Goss, W. M., & An, T. 2009, ApJ, 699, 186, doi: [10.1088/0004-637X/699/1/186](https://doi.org/10.1088/0004-637X/699/1/186)